

Object Detection Using Sim2Real Domain Randomization for Robotic Applications

Dániel Horváth^{1,2}, Gábor Erdős^{1,3}, Zoltán Istenes², Tomáš Horváth^{4,5}, and Sándor Földi¹

¹Centre of Excellence in Production Informatics and Control, Institute for Computer Science and Control, Eötvös Loránd Research Network in Budapest, Hungary

²CoLocation Center for Academic and Industrial Cooperation, Eötvös Loránd University in Budapest, Hungary

³Department of Manufacturing Science and Engineering, Budapest University of Technology and Economics in Hungary

⁴Department of Data Science and Engineering, Eötvös Loránd University in Budapest, Hungary

⁵Institute of Computer Science, Faculty of Science, Pavol Jozef Šafárik University in Košice, Slovakia

Robots working in unstructured environments must be capable of sensing and interpreting their surroundings. One of the main obstacles of deep learning based models in the field of robotics is the lack of domain-specific labeled data for different industrial applications. In this paper, we propose a sim2real transfer learning method based on domain randomization for object detection with which labeled synthetic datasets of arbitrary size and object types can be automatically generated. Subsequently, a state-of-the-art convolutional neural network, YOLOv4, is trained to detect the different types of industrial objects. With the proposed domain randomization method, we could shrink the reality gap to a satisfactory level, achieving 86.32% and 97.38% mAP₅₀ scores respectively in the case of zero-shot and one-shot transfers, on our manually annotated dataset containing 190 real images. On a GeForce RTX 2080 Ti GPU, the data generation process takes less than 0.5s per image and the training lasts around 12h which makes it convenient for industrial use. Our solution matches industrial needs as it can reliably differentiate similar classes of objects by using only 1 real image for training. To our best knowledge, this is the only work thus far satisfying these constraints.

Index Terms—Deep Learning in Robotics and Automation, Computer Vision for Automation, Localization, Sim2Real Knowledge Transfer

I. INTRODUCTION

IN recent years, a novel trend of new-generation intelligent manufacturing (NGIM) is emerging. It embodies the in-depth integration of new-generation artificial intelligence (AI) with advanced manufacturing technology such as robotics. It became the driving force of the fourth industrial revolution and it belongs to the human–cyber-physical system 2.0 (HCPS 2.0) framework. Contrary to traditional manufacturing where the robots work in structured environments and perform high-accuracy, repetitive tasks with less sensory inputs, an NGIM system is designed to be flexible and to take over as much intellectual and manual labor as possible. Thus, the human workforce can concentrate on more valuable creative work. [1]

Consequently, the main interest has been shifting towards adaptive robotic applications that can handle low-quantity customized products in an economically feasible way and human operators with different skills and abilities. Computer vision is highly researched as it is a useful tool in many fields of robotics such as pick-and-place manipulations, bin picking, robotic grasping, navigation of mobile robots, or quality assurance. As two examples for robotic arms, Zeng et al. [2] created a vision-based model that can predict parameters for grasping and throwing motion primitives through trial and error, and for mobile robotic applications, Alonso et al. [3] designed a model for real-time semantic segmentation of RGB images.

Deep convolutional neural networks (DCNNs) have been performing incredibly well on large public datasets such as

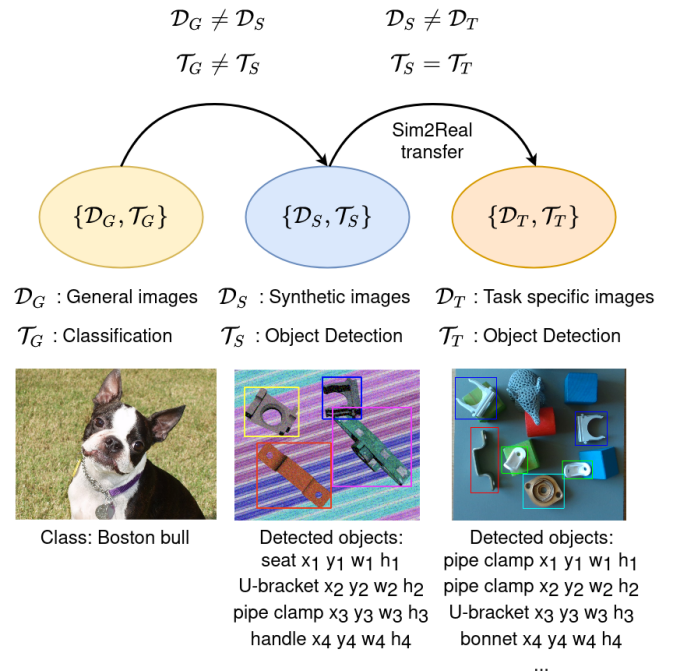


Fig. 1. The different phases of knowledge transfer. The picture of the boston bull on the bottom left corner of the figure is from ImageNet [4].

ImageNet [4] or MS COCO [5]. Having reached human-level performance in classification, the main focus of computer vision research has been shifted to object detection and led to networks such as the Faster R-CNN [6], Single Shot MultiBox Detector (SSD) [7], and YOLOv4 [8]. Even though these

networks are outperforming the traditional machine vision based methods by a significant margin, their application in robotic systems has its difficulties. One of the main obstacles in applying deep learning based models is that they need to be trained on a sufficiently large, domain-specific, and expertly labeled dataset.

Levine et al. [9] conducted two experiments in order to create a dataset of real images for their DCNN model to predict the success of robotic grasp attempts and to control these attempts. In the two experiments, they have recorded over 1.700.000 grasp attempts using between 6 and 14 robots at the same time. The data collecting process took several months. This example shows that, in general, collecting a dataset from the real world does not only require a huge amount of resources but is a time-consuming process as well.

The main motivation behind transfer learning is to overcome the aforementioned obstacle by transferring knowledge between tasks or domains [10], [11]. Sim2real transfer is a special case of transfer learning, where the source domain is the virtual simulation of the real world, while the target domain is the physical reality itself [12]. With sim2real knowledge transfer, the model can be trained in a virtual simulation, having the necessary amount of labeled synthetic data. In the case of computer vision, the images are rendered and the labels can be generated for them as well in a self-supervised way. Thus, the time-consuming process of data collection and labeling can be omitted. As the domain of the training and the test datasets are inherently different, *ceteris paribus*, the learned model will perform poorly on the target domain. The phenomenon of the performance loss from the simulation to the real domain is called the reality gap. Domain adaptation [13] and domain randomization [14], [15] are two ways to shrink this gap.

The contributions of this paper are as follows:

- A sim2real domain randomization method for object detection which describes a data generation process with our domain randomization methods, a model training phase, and an evaluation phase.
- A real-world dataset of 190 manually annotated images (RGB and depth) containing 920 objects of 10 classes that address the problem of high class similarity to validate our method. The dataset is publicly available alongside our code and can serve as a benchmark for object detection algorithms.
- For evaluation, we introduced an altered type of confusion matrix fit to object detection. It proved to be extremely useful for detecting and quantifying misclassifications which is the primary cause of performance loss in the case of similar classes.
- A real-world robotic implementation of the method as a proof of concept containing a ROS-based robot control system.
- Our implementations of our sim2real data generation and training module, and our robot control framework that are available at <https://git.sztaki.hu/emi/sim2real-object-detection> and https://git.sztaki.hu/emi/robot_control_framework. Both can be used as out-of-

the-box software modules for industrial robotic applications.

Results of the paper:

- We achieved 86.32% mAP₅₀ and 97.38% mAP₅₀ scores in zero-shot and one-shot transfers that show the usability of our methods even in the case of an industrial application where high reliability is crucial.
- Our experiments show that having even only one sample image from the target domain significantly improves the model's performance for similar classes.
- A thorough ablation study that focused on finding the key factors of the data generation process.

The industrial benefit of our work is a freely available tool that enables the user to train a CNN based model to object detection of different classes, having only the 3D models of the objects and optionally, for better performance, one annotated image consisting of the objects. In other words, with our sim2real domain randomization method, the user does not need to collect and annotate a huge dataset of images. Moreover, the process of data generation and the model training is automated and takes only around 13h.

In Section II and III, the problem statement and the related works are presented. In Section IV and V, our method is outlined with the evaluation metrics. In Section VI and VII, our dataset and our results are shown. Additionally, in Section VIII, a thorough ablation study of our method is presented. Finally, a real-world robotic implementation of our method is shown in Section IX.

II. PROBLEM STATEMENT

The main problem that this work aims to tackle is how to transfer knowledge efficiently between inherently different domains. More specifically, from simulation to real-world in the case of object detection. Object detection is a common computer vision problem in which the model gets an image as the input and localizes the center points, the widths and the heights of the bounding boxes, and also classifies all the objects on that image. Knowledge transfer belongs to the field of transfer learning. Additional attributes of the work that make the problem more challenging are the followings:

- Having zero or only 1 image from the real world.
- Having industrial objects that share similar features making it more challenging to properly classify them.

In the followings, we give a more detailed but still brief overview of transfer learning which is the main field of this paper.

Pan et al. [10] and Weiss et al. [11] in their surveys define transfer learning. A domain \mathcal{D} is defined with a feature space \mathcal{X} and a probability distribution $P(X)$, where $X = x_1, x_2, x_3, \dots, x_n \in \mathcal{X}$, while a task \mathcal{T} is defined with a label space \mathcal{Y} and a predictive function $f(\cdot)$. From a probabilistic point of view $f(\cdot)$ can be seen as $P(Y | X)$. Thus, a domain $\mathcal{D} = \{\mathcal{X}, P(X)\}$ and a task $\mathcal{T} = \{\mathcal{Y}, P(Y | X)\}$. Given a specific source domain and task pair $\{\mathcal{D}_S, \mathcal{T}_S\}$ and a specific target domain and task pair $\{\mathcal{D}_T, \mathcal{T}_T\}$, transfer learning can be defined as the process of increasing the performance of the

target predictive function $f_T(\cdot)$ with the help of knowledge gained from $\{\mathcal{D}_S, \mathcal{T}_S\}$, where $\mathcal{D}_S \neq \mathcal{D}_T$ or $\mathcal{T}_S \neq \mathcal{T}_T$.

An example of $\mathcal{T}_S \neq \mathcal{T}_T$ is when an image classifier that has been trained on a large public dataset is reused and altered to perform object detection on the same domain ($\mathcal{D}_S = \mathcal{D}_T$). In this case, the label spaces are different and consequently, the conditional probability distributions of the inputs and the outputs $P(Y | X)$ are disparate as well. Nevertheless, the marginal distributions of the inputs $P(X)$ are equivalent.

The other case of transfer learning is when $\mathcal{T}_S = \mathcal{T}_T$, but $\mathcal{D}_S \neq \mathcal{D}_T$, meaning that even though the tasks that must be performed are the same, the domains are different. Thus, the marginal probability distributions $P(X)$ and potentially the conditional probability distributions $P(Y | X)$ are different in the source and in the target domains. The former phenomenon is called the frequency feature bias while the latter is addressed as the context feature bias. To improve $f_T(\cdot)$, our aim is to extract the relevant (not domain-specific) knowledge from $\{\mathcal{D}_S, \mathcal{T}_S\}$. Thus, the model will perform well on the target domain (\mathcal{D}_T). If \mathcal{D}_S and \mathcal{D}_T are not related enough, negative transfer can happen meaning that the knowledge transfer does not improve or even decrease the performance of $f_T(\cdot)$.

Sim2real object detection is a special case of transfer learning where instead of real images drawn from the target domain, the model is trained on synthetic data, thus $\mathcal{D}_S \neq \mathcal{D}_T$. On the other hand, it performs the same task, namely object detection (on the same classes of objects), therefore $\mathcal{T}_S = \mathcal{T}_T$. Nevertheless, the model trained on synthetic data, *ceteris paribus*, does not work on real images as the domains are disparate. This phenomenon is called the reality gap and the main goal of sim2real transfer is to bridge this gap. In our case, the sim2real transfer is the second phase of the knowledge transfer, shown in Fig. 1.

Domain adaptation (DA) is an approach to diminish the reality gap. It attempts to transform one domain to the other domain or to transform both domains to a common domain. In the case of sim2real object detection, it usually means that photo-realistic images are generated for the training dataset. The more the generated images resemble the real ones, the more the difference between domains is reduced and thus, the performance on the real images is improved. Typical data generation models for domain adaptation usually build on the idea of variational autoencoders (VAE) [16] or generative adversarial networks (GAN) [17].

Domain randomization (DR) on the other hand introduces variability by applying artificial noise on the synthetic training images. The idea is that the added noise makes the model robust to different domains, as it does not overfit on the domain-specific characteristics, but learns the domain-independent underlying data representation. To look at it from another point of view, the different domains are seen as perturbed versions of one common domain. The general idea of introducing variance to simulation first comes from the work of Jacobi [18].

Other important concepts of transfer learning are the zero-shot and the one-shot transfers. In the context of object detection, zero-shot transfer means that not even one image is used from the target domain for training. On the other hand, in the case of one-shot transfer, only one or few images are

used from the target domain. A way to do one-shot transfer is to train the model on synthetic data and then fine-tune it on a couple of examples drawn from the target domain. In our one-shot transfer case, only one real image was used for training and we did not separate the process to training and fine-tuning as we mixed the copies of the real image and the synthetic images.

III. RELATED WORKS

In this section, the related works in sim2real knowledge transfer is presented in Section III-A. Furthermore, the different types of object detection models are presented in Section III-B.

A. Domain Randomization and Domain Adaptation

Tobin et al. [14] trained a modified version of VGG-16 [19] deep neural network architecture for object localization. They generated non-realistic synthetic RGB images randomizing the number and shapes of the distractor objects, the position and texture of all objects, the texture of the background, the position, orientation and the field of view of the camera, the number of lights in the scene, the position, orientation, and specular characteristic of the lights, and the type and amount of random noise added to images. The random textures were either a random single color, a gradient between two colors, or a checker pattern between two random colors. The following non-industrial objects were used: cones, cubes, cylinders, hexagonal prisms, pyramids, rectangular prisms, tetrahedrons, and triangular prisms. The images were rendered with the MuJoCo Physics Engine's built-in renderer [20] and no real images were used for training the model. They achieved around 1.5 cm accuracy in the real-world environment. Tobin et al. conducted a follow-up research [21] where they trained a deep neural network for grasp planning using only synthetic images and domain randomization and achieved an 80% success rate in a real-world environment.

Borrego et al. [22] presented their plug-in for the Gazebo simulator [23]. Introducing variation, they could narrow the reality gap between simulated and real-world data. In their case study, they detected three types of objects: box (cube), cylinder, and sphere. The simulated scenes contained a ground plate and a single light source. The objects were placed on a grid to prevent collusion (we found that introducing some disturbance for the placement of the object significantly increases the performance, see in Section VIII-D), but they were rotated randomly. Then the camera and the light source were moved to random positions. They used 4 different types of textures, namely: flat, gradient, checkerboard, and Perlin noise [24]. For training they used the SSD [7] and separately the Faster R-CNN [6] networks. With the two networks, they achieved 70% and 88% mAP₅₀ using 121 real images, respectively. Training the same networks with 9000 simulated images, they achieved 64% and 82% mAP₅₀, respectively. Interestingly, with the hybrid approach (using real and synthetic images), they accomplished 62% and 83% mAP₅₀, respectively. For all experiments, they used IOU 0.5 threshold (50 in mAP₅₀), and the test results were validated on 121 real images (different

from the 121 images used for the training). In a follow-up study [15] they conducted an ablation study where they found that the Perlin noise has a crucial influence on the model's performance. Furthermore, they have also fastened their data generation process, reaching the speed of 9000 full-HD images in roughly 1.5 hours (around 0.6s per image).

Pashevich et al. [12] trained manipulation policies in a simulation environment with an object localization proxy task. They used depth images simulated in PyBullet [25] and gathered with a Kinect-1 camera from the real world. For finding the best data augmentation transformation and their order, Monte Carlo Tree Search (MCTS) [26] was used. The transformations were selected from the Python Image Library (PIL). They evaluated the transformations individually and as a sequence as well. They found that, from all the examined transformations, the cutout transformation [27] performed the best on the real images (although in our experiments this was not the case for RGB images, see in Section VIII-E), and the best sequence of transformations was the followings: cutout, erasing an object, white noise, edge noise, scale, salt noise, posterize, and sharpness, in this order. With the aforementioned sequence, they achieved 1.09 ± 0.73 cm positional error in the real environment in the case of cubes of size 4.7 cm.

James et al. [28] trained an end-to-end robotic controller on synthetic data with domain randomization. The deep neural network based model's inputs were an image and the joint angles of the robot, and its output was the motor velocities. Its task was an abstract tidying manipulation, namely to put a cube into a basket. Similarly to [22] they used Perlin noise as a perturbation. They studied their model in dynamically changing illumination settings, in the presence of distractors, including human presence, novel cube size in test time, and in the case of a moving basket. They presented at least 75% of success rate in all conditions except in the case of a spotlight and in the case of a smaller cube in test time. In these cases, the model had a 56% and a 41% success rate, respectively.

Devo et al. [29] used domain randomization to train a target-driven visual navigation model. The goal was to find a specific object in a maze. They randomized the maze wall heights, the maze wall textures, the maze floor textures, the light color, the light intensity, and the light source angle. They achieved an average of 72% success rate in simulation and 46% in the real world. With their experiments, they showed that direct sim2real transfer is possible for this kind of problem as well. For simulation, the Unreal Engine 4 [30] was used.

Chen et al. [31] created the Domain Adaptive Faster R-CNN model for cross-domain object detection. They tackled the domain shift stems from image-level and instance-level shifts with an approach based on \mathcal{H} -divergence theory and adversarial training. Their study focuses on street images for self-driving cars where the domains are disparate due to the different camera types and setups, the different cities and the appearance of the objects, or the particular weather conditions. They also made some experiments with sim2real knowledge transfer as the model was trained on SIM 10k [32] and evaluated on Cityscapes dataset [33]. With their method, they improved the performance of the Faster-RCNN model from 30.12 AP₅₀ to 38.97 AP₅₀ in the case of the car class.

Sankaranarayanan et al. [34] proposed an unsupervised domain adaptation approach based on generative adversarial networks for semantic segmentation problems. Their work focuses on street scenarios. As the synthetic source domain, the SYNTHIA [35] and the GTA V [36] datasets, and for the target domain, Cityscapes dataset [33] were used. They achieved 36.1 mIOU and 37.1 mIOU scores transferring knowledge from SYNTHIA and GTA V, respectively. Without domain adaptation, the method scored 26.8 and 29.6 mIOU.

Tremblay et al. [37] generated synthetic images with domain randomization techniques to perform object detection of cars in street scenarios. They generated 100K images (maximum 14 cars each). The car models were randomly selected from 36 models. The models were evaluated on the KITTI dataset [38]. They trained three DCNN architectures, Faster R-CNN [6], R-FCN [39], and SSD [7], and they scored 78.1, 71.5, and 46.3 AP₅₀ on the single-class object detection problem. Interestingly, they yielded better results than training the same architectures on the virtual KITTI dataset [40] which has a high correlation to the KITTI dataset. The performance could be improved by fine-tuning the models on real images. With 6000 real images, the performance of the Faster R-CNN model reached 98.5 AP₅₀.

Hinterstoisser et al. [41] inserted 3D models of objects on real image, using OpenGL with Phong shading [42] for rendering. They allowed small perturbation of the ambient, the diffuse, the specular parameters, and the light color. They added Gaussian noise and a blur with Gaussian kernel to integrate the objects with the background better. For training, they primarily used a Faster R-CNN model with freezing the weights of the feature extractor. Freezing the weights significantly improved the performance of the model (Although, afterward [37] reported opposite effect in their case).

Zhang et al. [43] propose an adversarial discriminative sim2real approach to transfer visuo-motor policies. They demonstrated their method in a table-top object reaching task. A blue cuboid object needed to be reached with a velocity-controlled 7 DoF robot arm. With their method, they could reduce the real data requirement by 50% and they achieved a 97.8% success rate and 1.8 cm control accuracy.

Clever et al. [44], [45] propose a method to predict human position (resting on a bed) and contact pressure from depth data and the gender information. Their proposed methods achieved 3.837 MSE(kPa²) trained on 97K synthetic images. In comparison, the same method reached 3.151 MSE(kPa²) trained on 11K real images and 2.849 MSE(kPa²) trained on both real and synthetic images (108K). For evaluation they used the SLP dataset [46].

Gomes et al. [47] proposed a simulated model for the GelSight tactile sensor. Having computed the heightmap of the elastomer, the internal illumination of the elastomer is calculated. They also demonstrated the usefulness of their model with a sim2real classification task. They created 12 texture maps that resembled the textures of real objects and randomly perturbed them on the captured synthetic data improving the classification accuracy from 43.76% to 76.19%.

There are many parameters of the listed works that make it challenging to compare them with each other and also with

our work. Nevertheless, to make them more comparable, the summary of these works can be seen in Tab. I. The main factors are the input type, the domain, the model, and the amount of synthetic and real images that were used to train the model. In general, the limitations of the related works that are close to ours are the followings:

- The classification part of the problem is less challenging as they use easy shapes such as cubes, spheres, and cones or even have only 1 class.
- Having considerably more synthetic and real images for training.

Even though these works use transfer learning (domain adaptation or domain randomization) to shrink the reality gap, they do not solve the same machine learning problem (the input, the output, and the domain) and might use different models as well. All of this needs to be taken into consideration when someone compares them.

B. Object Detection

While the thorough survey of the object detection algorithms and the history of the field is not in the scope of this paper, we refer the reader to standard surveys such as the work of Zou et al. [53].

DCNN architectures can be categorized into two groups: two-stage detectors and one-stage detectors. Two-stage detectors have a proposal detection stage where a set of bounding box candidates are generated and a verification stage where these bounding boxes are separately evaluated whether they contain an object of a specific class. Examples of these networks are R-CNN [54], SPPNet [55], Fast R-CNN [56], Faster R-CNN [6].

On the other hand, in the case of one-stage detectors, a single neural network is applied to the full image that predicts the bounding boxes straight away. The slow detection time which is the biggest disadvantage of the two-stage detectors, can be overcome with the one-stage approach. Detection time is crucial for many applications especially but not exclusively in the field of robotics or self-driving cars. Redmon et al. proposed the first one-stage detector in 2015 called YOLO [57] which became the first real-time object detector. In following updates they introduced its second [58] and third versions [59]. Single Shot MultiBox Detector (SSD) [7] and RetinaNet [60] are two other popular one-stage detectors.

Bochkovskiy et al. [8] created the fourth version of YOLO aiming to improve the accuracy of the model and still keeping an optimal accuracy-speed trade-off. With the CSPDarknet-53 [8] backbone, they could achieve 65.7% mAP₅₀ for the MS COCO dataset [5] and around 65 FPS speed on a Tesla V100. In comparison, on the same dataset, SSD with VGG-16 [19] backbone performed 48.5% mAP₅₀ and RetinaNet with ResNet-101 [61] backbone achieved 57.5% mAP₅₀.

IV. METHOD

In this section, having presented the proposed sim2real knowledge transfer in Section IV-A, the data generation module is described in Section IV-B and the training module is detailed in Section IV-C. The implementation is freely available: <https://git.sztaki.hu/emi/sim2real-object-detection>.

A. Sim2Real Knowledge Transfer

The flowchart diagram of our data generation, training, and evaluation process is depicted in Fig. 2. It can be broken down into functionally separable tasks. The data generation process creates randomized and post-processed synthetic images of given objects. It also automatically generates the annotations for the images. Thus, the output of the data generation process is a set of images paired with their labels grouped into a training and a validation dataset.

To train the model (with the set of hyperparameters), only the images from the training dataset are used. As the initial layers of the neural network perform low-level image processing tasks such as detecting contours, lines, or edges, we utilized a pretrained image classifier model as a feature extractor of our object detector. This is the first phase of our knowledge transfer, depicted on the left side of Fig. 1. The knowledge transfer goes from $\{\mathcal{D}_G, \mathcal{T}_G\}$, where \mathcal{D}_G is the domain of the dataset of general public images and \mathcal{T}_G is classification, to $\{\mathcal{D}_S, \mathcal{T}_S\}$, where \mathcal{D}_S is the domain of synthetic images (source domain of the sim2real knowledge transfer) and \mathcal{T}_S is object detection. Here, $\mathcal{D}_G \neq \mathcal{D}_S$, and $\mathcal{T}_G \neq \mathcal{T}_S$. The second phase of knowledge transfer is the sim2real transfer which goes from $\{\mathcal{D}_S, \mathcal{T}_S\}$ to $\{\mathcal{D}_T, \mathcal{T}_T\}$, where \mathcal{D}_T is the domain of our industrial environment (target domain) and \mathcal{T}_T is object detection. Here, $\mathcal{D}_S \neq \mathcal{D}_T$ but $\mathcal{T}_S = \mathcal{T}_T$. As described previously, the pretrained network possesses some learned knowledge from the domain of a given general public dataset (\mathcal{D}_G). As these datasets are from a general domain and do not have the classes that we need, the pretrained knowledge does not contain direct information about the target object. Consequently, $\mathcal{D}_G \neq \mathcal{D}_S \neq \mathcal{D}_T$. Even though $\mathcal{D}_G \neq \mathcal{D}_T$, the characteristics of the domains are similar. Thus, on Fig. 1 and Fig. 2, the domain of general public images is marked with a different shade of orange (as the task-specific real images).

B. Data Generation

The data generation process is responsible for the creation of synthetic images paired with accurate automatic ground-truth annotations. In several stages of this process, artificial random perturbations are applied as domain randomization techniques.

1) Framework

For data generation, the PyBullet [25] physics simulator was used since it has an easy-to-use, intuitive API, including an image renderer tool, and an integrated physics simulator where the gravitational force can be easily simulated. It is important to mention that one of the biggest advantages of domain randomization over domain adaptation is that it is generally faster as images do not need to be photo-realistic. In our case, we could achieve less than 0.5s per image (generation) on a GeForce RTX 2080 Ti GPU. With 4000 images it is around 33 minutes. In general, the time of dataset generation is an important aspect of the method as in the industry, on many occasions, it is not feasible to wait long hours or even days to start the training. As an example, instead of 33 minutes, the aforementioned 4000 images would cost more than 66h if 1 image is rendered in 1 minute which is plausible in the case of photo-realistic images. Having generated the dataset,

TABLE I
SUMMARY OF RELATED WORKS

Work	Problem	Input	Domain	DR/DA	Base Model	Simulator	Synthetic Images	Real Images	Results	
Tobin [14]	Detection	RGB	Shapes	DR	VGG-16	MuJoCo [20]	5K-50K	0	1.5 cm	
Tobin [21]	Grasping	Depth	YCB [48]	DR	CNNs	MuJoCo [20]	2K / obj	0	80% success	
Borrego [22]	Detection	RGB	Shapes	DR	Faster R-CNN	Gazebo [23]	9K	0	82% mAP ₅₀	
							9K	121	83% mAP ₅₀	
							9K	0	64% mAP ₅₀	
							9K	121	62% mAP ₅₀	
Pashevich [12]	Detection	Depth	Cubes	DR	ResNet-18	PyBullet [25]	2K	0	1.09±0.73 cm	
							-	0	15/20	
James [28]	Pick-and-place	RGB, joints	Cube	DR	CNNs	V-REP [49]	100K-1M	0	≥41% success	
Devo [29]	Navigation	2xRGB	-	DR	CNNs	UE4 [30]	540K	0	46% success	
Chen [31]	Detection	RGB	Street	DA	Faster RCNN	-	10K	3K(unlab.)	38.97 AP ₅₀	
Sankaranarayanan [34]	Segmentation	RGB	Street	DA	GAN	-	25K	5K(unlab.)	37.1 mIOU	
Tremblay [37]	Detection	RGB	Street	DR	Faster R-CNN	UE4 [30]	100K	0	78.1 AP ₅₀	
							100K	6K	98.5 AP ₅₀	
							R-FCN	100K	0	71.5 AP ₅₀
							SSD	100K	0	46.3 AP ₅₀
							CNNs	20K	0	ca. 70% mAP ₅₀
Hinterstoisser [41]	Detection	RGB	Household	DR	CNNs	OpenGL	20K	0	ca. 70% mAP ₅₀	
Zhang [43]	Grasping	RGB	Cube	DR	VGG-16	V-REP [49]	3K	93 + 186 (unlab.)	97.8% success, 1.8 cm accuracy	
Clever [44], [45]	Contact pressure	Depth	Humans	DR	CNNs	DART [50], FleX [51], Pyrender [52]	97K	0	3.837 MSE(kPa^2)	
							97K	11K	2.849 MSE(kPa^2)	
Gomes [47]	Classification	RGB	Shapes	DR	ResNet-50	Gazebo [23]	1470	0	76.19% accuracy	
Our results	Detection	RGB	Industrial	DR	YOLOv4	PyBullet [25]	4K	0	86.32% mAP₅₀	
							2K	1	97.38% mAP₅₀	

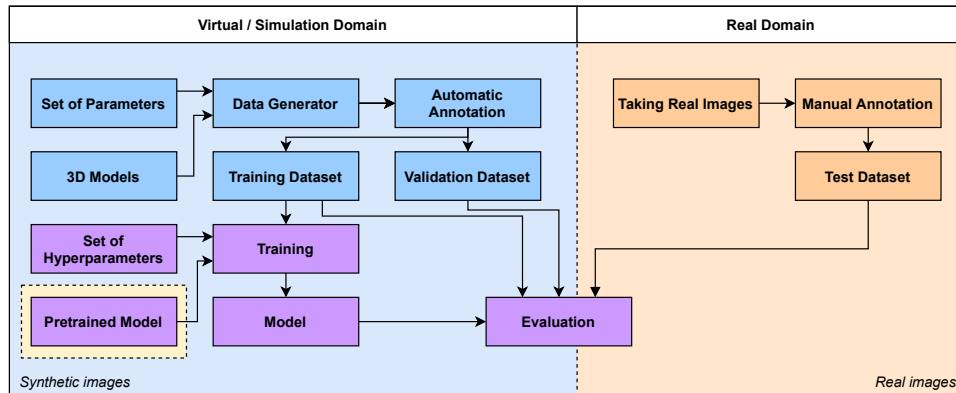


Fig. 2. The flowchart diagram of our data generation, training, and evaluation process. The blue and orange boxes depict the data generating and data gathering steps. The purple boxes represent the steps of training and evaluation.

the training lasts around 12h, thus a whole generation and training process can be automatically executed in around 13h.

2) Object Generation

The framework is capable of placing any type of object into the simulation if its 3D description file is given. In the case

of industrial applications, which is the aim of this research, these 3D models are easily accessible.

The most relevant input parameters of the object generation process are summarized in Tab. II and the process works as described in the followings:

- A horizontal plane is placed at the vertical $z = 0$ position.
- According to the grid size (n) and the grid spacing (d) parameters, the x and y coordinates of the grid points are set.
- The vertical $z > 0$ coordinates of the grid points are set by z_{pos} .
- The objects are not placed exactly at the grid points. The x , y , and z coordinates of the objects are drawn from a uniform distribution in which the center point is a given grid point and the limits of the distribution are set by ϵ_{pos} .
- Once the object selection is performed, the appropriate 3D model of the object is loaded into the specific coordinates. There are predefined weights that describe the probability that a specific object is being selected. Furthermore, a distracting cuboid object (which is not in any of the classes) or a void object (leaving that grid point empty) can be selected. The sizes of the distracting objects are also individually randomized. The aforementioned probabilities are set by $P_{objects}$.
- The objects are also randomly rotated around the x , y , and z axes, described by a uniform distribution whose limits are set by ϵ_{rot} .
- The objects and the ground plane are given some random textures drawn from three public datasets [62], [63], [64], with the probability of $P_{texture}$. Random RGB colors are given to the objects (or to the ground plane) that do not get any textures. Some examples of the textures are shown in Fig. 3.
- Before rendering the image, the objects are dropped down from $z > 0$ to the ground plane. Thus, the objects will be captured in a natural stable position. The simulation of the free fall takes around 0.05-0.1s per scenario (with every step included, the generation of an image with its label is around 0.45-0.5s).



Fig. 3. Some examples of the used textures. [62], [63], [64]

3) Image rendering

For rendering an image, the camera position, its inner parameters, and additional parameters must be set. The most relevant parameters of the image rendering are presented in Tab. III. The algorithm works as follows:

TABLE II
THE MOST RELEVANT INPUT PARAMETERS OF THE DATA GENERATOR MODULE IN TERMS OF OBJECT GENERATION

Notation	Type	Description
n	scalar	The grid size ($n \times n$).
d	scalar	The grid spacing. The distance between the adjacent grid points
z_{pos}	scalar	The position of an object in z direction.
ϵ_{pos}	array	Contains the proportionate (to the grid spacing) perturbation limits in the directions of x , y , and z around the center point.
ϵ_{rot}	list of arrays	ϵ_{rot} describes the lower and upper bounds for the possible rotation angles of the directions in x , y , and z .
$P_{objects}$	array	Contains the selection probabilities of the given objects (including the distractor object and the void object).
$P_{texture}$	scalar	The probability that a specific object or the ground plane is having a random texture. Otherwise, it gets a random color.

TABLE III
THE MOST RELEVANT INPUT PARAMETERS OF THE DATA GENERATOR MODULE IN TERMS OF IMAGE RENDERING

Notation	Type	Description
T_{pos}	list of arrays	The camera points to a certain point in the 3D space. The arrays of T_{pos} describe the lower and upper bound of the camera target point in the directions of x , y , and z .
C_{pos}	list of arrays	The pose of the camera is defined by 3 parameters: the rotation angle around the global z axis, the pitch angle from the global xy -plane and the distance between the camera and the target point. The arrays of C_{pos} describe the lower and upper bound of these parameters.
R_{width}	array	The R_{width} parameter describes the lower and upper bound of image width in pixels.
R_{height}	array	The R_{height} parameter describes the lower and upper bound of image height in pixels.
FOV	scalar	The field-of-view of the camera.
I_{type}	scalar	Three types of images can be rendered: 3-channel RGB images, depth images, 4-channel RGB-D images.

- The camera is placed in a randomized position pointing to a random point around the center of the grid defined by C_{pos} and T_{pos} . The randomization is constrained in a way that all the objects' center points must appear on the rendered image.
- The camera field-of-view (FOV) and its additional intrinsic parameters are set. The image width and height are drawn from a uniform distribution defined by R_{width} and R_{height} .
- With the built-in renderer, the RGB, D (depth), or RGB-D images can be taken easily, defined by I_{type} . RGB-D images can be created by concatenating the RGB and the D images. For one layout (object generation), only one image is taken.

4) Label Generation

Having generated the objects and rendered the image, the ground-truth bounding box (BB) parameters must be computed. For different CNNs, the format is different, but it is generally true that the bounding box parameters describe all the objects in an image as follows:

- The center point (x and y) of the object.
- The width, and the height of the bounding box.
- The class of the object.

The aforementioned ground-truth generation is an automatic process involving a coordinate transformation from the simulation 3D world coordinate system to the image 2D coordinate system.

The 4×4 transformation matrix is the matrix multiplication of the camera's view matrix and its projection matrix. To transform a point from the world coordinate system to the image space, it must be multiplied with this transformation matrix and then scaled back by its fourth coordinate to get the true projection. For a detailed explanation of the projection, we refer the reader to [65].

In the framework, we implemented two ways of computing the bounding boxes. The two approaches differ in the number of points that are transformed into the image space. One approach transfers only the 8 points of the world 3D axis-aligned bounding boxes (AABB), which is available in the PyBullet simulator, whereas the other transforms all the points of the objects to the image space. Henceforward, we refer to the former approach as the 8-point method and the latter as the all-point approach. Having the transformed points, the second part of the algorithm is the same in both cases, the minimum and maximum values in x and y directions are selected to define the limits of the BBs. The center point can be computed as the arithmetic means of the minimum and maximum values. As a result, the latter method gives tighter, more accurate bounding boxes at the expense of the extra calculations.

5) Post-Processing

The technique of domain randomization was performed in many steps of the previously defined synthetic image generation process. In the post-processing phase, as a domain randomization technique, additional artificial noise is introduced to alter the images. The images are perturbed with a randomized multi-color pepper-and-salt noise and a Gaussian blur. Furthermore, as Pashevich et al. [12] found the rectangle cutouts useful for depth images, experiments were made with rectangle, and additional circle, and line cutouts as well on our RGB images. The types of noises that were applied are shown in Fig. 4, described in Tab. IV, and applied in the following order:

- 1) rectangle cutout,
- 2) circle cutout,
- 3) line cutout,
- 4) multi-color pepper-and-salt,
- 5) Gaussian blur.

The goal with post-processing is to force the model not to learn the synthetic domain-specific characteristics, but to try to learn the domain-independent underlying data representation. The ablation study on our experiments, described in

TABLE IV
THE TYPES OF NOISES IN POST PROCESSING

Name	Description
Multi-color pepper-and-salt	With a given p probability, every channel of every pixel is set either to zero or to the maximum value.
Gaussian blur	With a given p probability, the whole image is blurred with a randomized filter size.
Cutout	A given number of rectangle, circle, or line shaped regions with randomized dimensions and at randomized positions are colored to a random RGB value.

Section VIII shows that having the post-processing module undoubtedly improves the models' performance on the test dataset. Nevertheless, it also reveals that the added cutout noises did not improve the performance compared to the default Gaussian blur and multi-color pepper-and-salt noise.

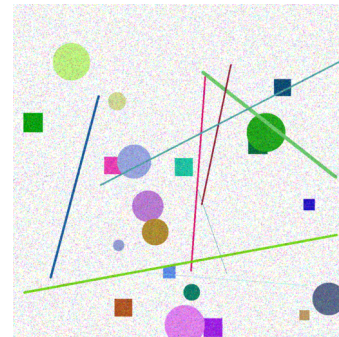


Fig. 4. Post-process transformation on a blank image.

C. Training

Even though the method would work with any given CNNs, for this research, we have chosen the YOLOv4 [8] architecture for the following reasons:

- It has the best speed and accuracy trade-off which makes it a good fit for robotic applications. It also has a tiny version, that makes it possible to run it real-time even on a microcomputer such as a Raspberry PI or NVIDIA Jetson Nano.
- Its training framework contains additional advanced data augmentation tools. For more information, we refer the reader to [8]. These tools help to introduce further perturbation to the system.

For the training, a pretrained model trained on ImageNet [4] is used. There are some hyperparameters for the advanced data augmentation tools that significantly affect the success of the training. The most relevant ones are shown in Tab. V, keeping the original names of the parameters.

In Section VIII-F we present our results of our method changing only the object detection model from YOLOv4 to Faster R-CNN.

TABLE V
THE MOST RELEVANT ADVANCED DATA AUGMENTATION TOOLS IN THE TRAINING PROCESS

Name	Description
Angle	Randomly rotates images.
Saturation	Randomly changes the saturation.
Exposure	Randomly changes the brightness.
Hue	Randomly changes the hue color channel.
Mosaic	Use 4 images in one Mosaic data augmentation technique [8].
Jitter	Randomly changes the size of the images and its aspect ratio.
Random	Randomly resizes network size after each 10 batches.

V. EVALUATION

In this section, we outline the metrics that we use to evaluate our models. First, we define how we measured the reality gap, then we introduce our altered version of the confusion matrix, and last, we outline some further details of our evaluation process.

To evaluate the solution of the classical machine learning problem, (training and evaluation on the same domain), real-world images would not be needed. In this case, the performance is assessed on the generated validation dataset that is not used for training but coming from the same distribution $P_{train}(X) = P_{valid}(X)$. The solution can be assessed by the value of the model’s mAP score on the valid dataset, and the capability of generalization (within the specific domain) can be measured by comparing the model’s performance on the train and on the valid datasets, as in Eq. 1.

$$G_{ML} = mAP_{train} - mAP_{valid} \quad (1)$$

To evaluate the performance of the knowledge transfer, a manually annotated test set of real images is needed. In this case, $P_{valid}(X) \neq P_{test}(X)$. We expect that the given model performs notably worse on the test set than on the valid and on the train sets. To measure the magnitude of the reality gap, we can define it as the difference of the model’s performance on the validation and on the test sets, as shown in Eq. 2.

$$G_{reality} = mAP_{valid} - mAP_{test} \quad (2)$$

Furthermore, we adapt the confusion matrix measure from the field of image classification to object detection and use it as an additional performance measure. The adaptation works as described in the following:

- Adding an extra row and an extra column to the classical confusion matrix. Thus, there are $c+1$ rows and columns, where c is the number of classes. The additional row represents the objects that are not predicted to any of the classes but actually belong to one class. On the other hand, the additional column of the matrix represents the cases when the model predicted an object of a class in a position where there should not be any object.
- The values of the diagonal are the correct predictions. For simplicity, the last element of the diagonal is zero.

This element should contain the number of objects that are not on the images and so the model rightfully did not find them, which does not have any meaning.

- As more than one prediction can belong to one ground-truth object, a given ground-truth object appears in the matrix as many times as many predictions are paired with it. Therefore, contrary to the traditional confusion matrix, the sum of all elements in the matrix will not necessarily be equal to the sum of all ground-truth objects or predictions.

The described adapted confusion matrix is proven to be useful for detecting and quantifying misclassifications which is especially important in the case of similar classes as in this case, this is the primary cause of performance loss. Examples are shown in Section VII on Fig. 14 and Fig. 20.

Presenting our results in Section VII, for every generated dataset, three independent training sessions were conducted resulting in three different models (sets of weights) in order to measure the deviance of the training process. When the average performance of the models is mentioned, it refers to the arithmetic mean of the results of these three models. We also use the F_1 score measure, which is defined as the harmonic mean of the precision and the recall values.

VI. DATASET

In this section, the created dataset is presented on which our method is validated, shown in Section VII.

Ten industrial parts were selected for the dataset. Object diversity and also object similarity were the two major points of consideration. The former helps us to evaluate the models’ detection performance for various types of objects, whereas the latter is important in assessing the models’ classification performance. In general, it is easier to misclassify objects with similar features. Thus, this problem can be considered to be more challenging than the detection of less complex and fairly different shapes such as cubes and spheres. The selected objects are depicted on Fig. 5 and their virtual counterparts on Fig. 6. These images are samples of $X \in \mathcal{X}$ drawn from two different $P(X)$ probability distributions. The virtual images are from the probability distribution P_S of $\mathcal{D}_S = \{\mathcal{X}, P_S(X)\}$, while the real images are from the probability distribution P_T of $\mathcal{D}_T = \{\mathcal{X}, P_T(X)\}$.

As it can be seen, on one hand, objects of different sizes, shapes, colors, and materials were selected to increase diversity. On the other hand, some objects share similar characteristics, such as circle-shaped holes. Furthermore, two parts, the bonnet (#7) and the body (#8) were chosen because of their high level of similarity, shown in Fig. 7.

Constructing the dataset, 190 real images of 920 object instances were taken with different layout and illumination settings. The images were captured with an Intel RealSense D435 camera. For easy and fast image capturing, a frame was designed that holds the camera 310 mm from the ground. There is a $300 \times 210 \times 10$ mm light blue wooden base that supports the frame. The parts were put on this area. Purposefully, on the images, not only this base area can be seen but

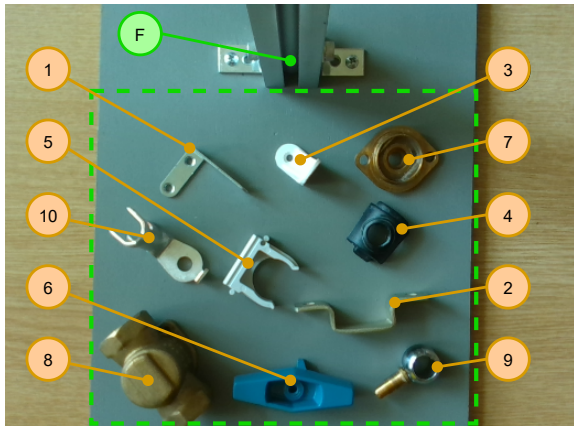


Fig. 5. The selected industrial parts for the dataset. Their names in order of their identifier numbers are the following: 1. L-bracket, 2. U-bracket, 3. angle bracket, 4. seat, 5. pipe clamp, 6. handle, 7. bonnet, 8. body, 9. ball, 10. cable shoe. With the letter 'F' the camera holder frame is signed. With the green dashed lines, the borders of the cropped images are shown.

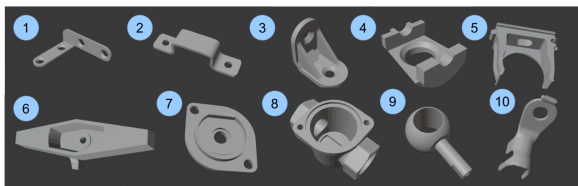


Fig. 6. The 3D models of the selected industrial parts of the dataset. Their names in order of their identifier numbers are the following: 1. L-bracket, 2. U-bracket, 3. angle bracket, 4. seat, 5. pipe clamp, 6. handle, 7. bonnet, 8. body, 9. ball, 10. cable shoe. Their scaling factors are different for better visualization.

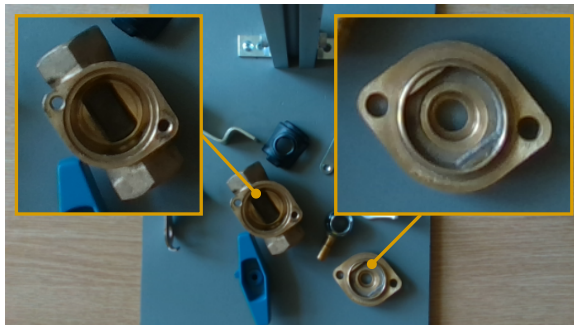


Fig. 7. The similarity of the body and the bonnet objects.

the background (tabletop) as well. To have a slightly different dataset as a reference, we also transformed the aforementioned dataset by cropping the images to fit in the wooden base. The cropped area is signed with dashed green lines on Fig. 5. Some examples of cropped images are shown in Fig. 15 and Fig. 21.

The annotations for the test dataset were labeled manually and saved in the YOLO annotation format. As it contains all the necessary bounding boxes and class information, other annotation formats can be generated from them. We emphasize that these images of real objects were not used at any point for training the models, except in the case of one-shot knowledge transfer. In this case, only one real image was used. The experiment of one-shot transfer is presented in Section VII-B.

TABLE VI
SUMMARY OF THE TEST DATASET

ID	#Img	#Obj	Object density	Illumination	Distractors
A	53	52	0.98	Normal	No
B	19	182	9.58	Normal	No
C	20	144	7.20	Spot light	No
D	21	264	12.57	Normal	No
E	22	135	6.14	Normal	Yes
F	55	143	2.60	Normal	No.
SUM	190	920	4.84		

For all images, the matching depth images are recorded as well. The depth images are transformed in a way that each pixel point of the RGB image can be associated with the same pixel point of the depth image (the transformation is necessary as the camera's field-of-views for RGB and for depth images are different). Thus, all the annotations for the RGB images are the same for the depth images. Even though the depth images were not used in this research, this additional data can be valuable for later use or for other researchers.

The test dataset is summarized in Tab. VI. In Group A, there is only one object on every image (except one image without any objects). In Group B, on every image, there are many objects, but no class is presented more than once. In Group C, from one side, a spotlight illumination is applied. Thus, the models' robustness to illumination settings can be tested. Group D includes images, crowded with parts. In Group E, distractor objects (cubes, cylinders, triangular prisms, and a 3D-printed elephant) are placed in the scene. Finally, in Group F, in every picture, only 1 class is presented, however, unlike in group A, there are more instances of this class on every image.

The group-wise class distributions are depicted in Fig. 8. As it can be seen, the classes are relatively equally distributed in the groups. Even though in the mAP metric, the mean of the classes is calculated, thus it is less influenced by class imbalance, it is advantageous to create an equally distributed test dataset. Obviously, for training, which can be sensitive to class imbalance, the synthetic data is generated with a random selection of objects, thus eliminating any notable class imbalance. The dataset can be downloaded from the project's repository: <https://git.sztaki.hu/emi/sim2real-object-detection>.

VII. RESULTS

In this section, we present the strength of our sim2real object detection method by applying our method described in Section IV for the problem presented in Section VI.

A. Zero-shot transfer (ZST)

The best performing zero-shot transfer model (ZST_BEST_1)¹ achieved 86.32% mAP₅₀ on the cropped

¹ZST: zero-shot transfer; BEST: the best data generation method; index: the index number of the training session

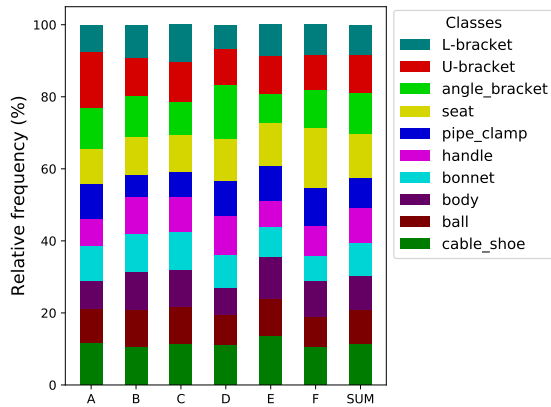


Fig. 8. Statistic of the class distribution of the test dataset.

test dataset. For data generation, a 2×2 grid with fixed z positions and a placement disturbance of $\pm 10\%$ of the grid spacing was set in the horizontal directions. The simulation of gravity was enabled and the objects (including distractors and empty places) were selected with equal chance. The objects had random textures with the probability of 0.8 and a random color with the probability of 0.2. The camera target position and field-of-view were fixed at 45 degrees and pointing towards the center of the grid. However, the pitch of the camera was randomized between -0.17 and 0.17 radian. The width and height of the images are chosen randomly, independent of each other. Their values lie between 640 and 1300 pixels. For post-processing, the multi-color pepper-and-salt noise and the Gaussian blur were used with the probability of 1.0 and 0.5, respectively. 4000 images were generated for the training dataset, and 200 for the validation dataset. The evaluation of the model's performance on the training set was measured only on the first 200 images of the training set. Two examples of the generated synthetic images are shown in Fig. 9

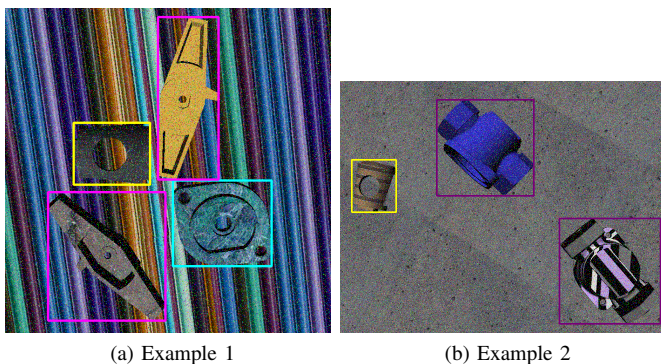


Fig. 9. Two examples of generated synthetic images with the automatically generated annotations. The bounding boxes are shown here but evidently they are not on the images.

The precision-recall curves of the three ZST_BEST models (from the three training sessions) are shown in Fig. 10. As both the training and validation mAPs are close to 100%, it can be stated that the solution of the classical machine learning problem is satisfactory. Furthermore, observing the sim2real

transfer, it can be seen, that the models do not only have a relatively good performance on the test data, but they also have little variance. Moreover, the models perform relatively similarly on the original and on the cropped images which shows the good robustness of the method. The F_1 score is depicted in Fig. 11. It shows that while the performance of the model on the cropped images is not affected by the threshold, the models work better with higher threshold values on the original images.

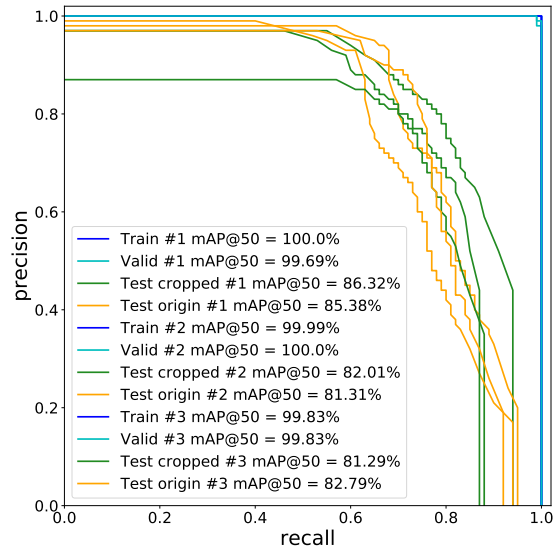


Fig. 10. The precision-recall curves of the ZST_BEST models. The train and valid scores are overlapping and relatively close to the perfect 1.0 values.

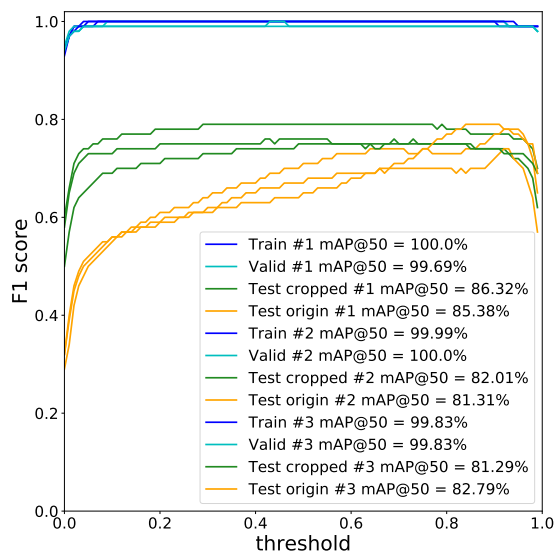


Fig. 11. The F_1 scores of the ZST_BEST models.

The models' performance on the different groups of the test dataset described in Tab. VI are presented in Tab. VII. The performance is relatively stable across the different types of scenes. Group D, containing the most crowded images performs just slightly worse than the others. In the case of the

TABLE VII
THE MAP₅₀ SCORES OF THE ZST_BEST MODELS IN THE DIFFERENT TEST GROUPS

ID	Train #1		Train #2		Train #3		AVG.	
	Orig.	Crop.	Orig.	Crop.	Orig.	Crop.	Orig.	Crop.
A	82.43	95.71	75.85	84.86	83.97	87.00	80.75	89.19
B	89.27	86.48	85.70	80.26	86.00	81.18	86.99	82.64
C	85.02	82.41	86.69	82.27	83.97	79.11	85.23	81.26
D	84.50	83.94	82.54	80.07	79.89	76.58	82.31	80.20
E	87.22	85.05	82.99	84.91	82.02	83.52	84.08	84.49
F	86.03	95.11	79.63	87.50	88.41	91.68	84.69	91.43

original images, group A has a relatively low performance. This is due to the fact that the model occasionally falsely identify the brackets of the camera holder frame (at the two sides of the camera holder frame which is displayed in Fig. 5, signed with the letter 'F') as L-brackets which is not surprising as these parts look similar. As group A has the lowest number of objects, this phenomenon affects the results the most in this case. The cropped images, as it is shown in Fig. 5, do not contain this part of the image.

Furthermore, it is worth investigating the models' performance for the different classes. The data presented in Tab. VIII and the average results are shown in Fig. 12. Looking at the dataset of cropped images (green) it can be seen that 6 out of 10 classes perform above 92%, one class is relatively close to them with 87.94% AP₅₀, two classes have relatively worse results with 69.54% and 67.18% AP₅₀, and one class called the bonnet has significantly worse performance with 30.72% AP₅₀. Otherwise, for all the classes the performance on the validation dataset is close to 100%. It means that the performance loss is not caused by the unsuccessful solution of the classical machine learning problem, but the existence of the reality gap. As most of the classes have relatively good APs, the one bad class is out-weighted by them in the mAP calculation.

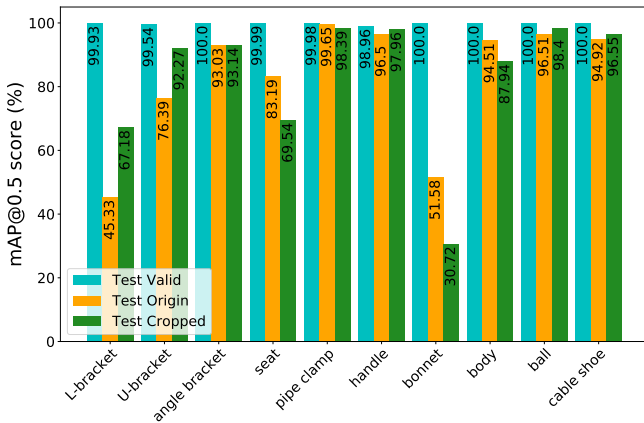


Fig. 12. The average mAP₅₀ scores of the ZST_BEST models in the different classes.

In order to investigate the aforementioned problem, the

TABLE VIII
THE MAP₅₀ SCORES OF THE ZST_BEST MODELS FOR THE DIFFERENT CLASSES

ID	Train #1		Train #2		Train #3		AVG.	
	Orig.	Crop.	Orig.	Crop.	Orig.	Crop.	Orig.	Crop.
1	41.45	63.15	45.26	71.85	49.28	66.54	45.33	67.18
2	76.34	91.66	77.51	91.58	75.32	93.56	76.39	92.27
3	94.14	93.14	91.56	93.17	93.39	93.11	93.03	93.14
4	84.96	77.71	71.88	60.16	92.72	70.74	83.19	69.54
5	99.82	95.72	99.37	99.49	99.76	99.97	99.65	98.39
6	95.77	98.21	94.82	97.53	98.90	98.14	96.50	97.96
7	71.77	54.26	52.39	22.01	30.57	15.90	51.58	30.72
8	96.51	92.13	93.77	92.23	93.26	79.46	94.51	87.94
9	97.13	99.03	94.27	96.89	98.14	99.27	96.51	98.40
10	95.87	98.19	92.32	95.22	96.57	96.24	94.92	96.55

class-wise precision-recall graph of ZST_BEST₁ is shown in Fig. 13. As it can be seen, the bonnet, the L-bracket, and the seat are the worst classes in consistence with Fig.12.

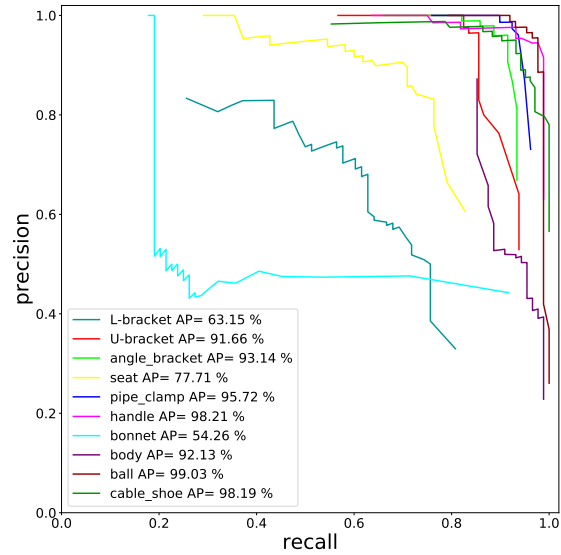


Fig. 13. Class precision-recall curves of the ZST_BEST₁ model on the cropped images.

The proposed confusion matrix depicted in Fig. 14 is essential to find the root causes of the models' weaknesses. In most cases, the objects are detected and classified to the good class (diagonal). However, several objects of L-bracket and seat are not detected (36 and 49 examples) and many bonnets are classified as body objects (62 instances). The problem between these two objects is not surprising considering the high level of similarity of the two objects shown in Fig. 7. In general, this representation of the results is not only reinforced the aforementioned assumptions of class performances but also shows the underlying reason behind the lack of performance in their cases.

Finally, having presented the quantitative evaluation, there

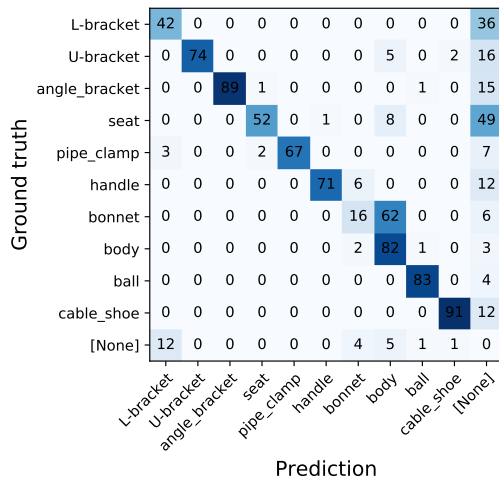


Fig. 14. Confusion matrix of the ZST_BEST₁ model on the cropped images with 0.8 threshold.

TABLE IX
TRAINING DATASETS

	Synthetic images	Real images
ZST	4000	0
OST	2000	1 (copied x2000)

are two examples for qualitative evaluation as well. Fig. 15 shows an accurate and an inaccurate example, both with the threshold of 0.8. Whereas, the model could accurately find and classify all the parts even in the presence of distractor objects in Fig. 15 (a), it fails to detect two instances of the seat class and puts the bonnet object to the body class in Fig. 15 (b).

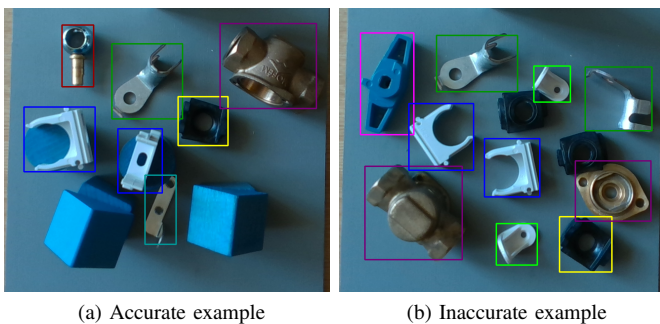


Fig. 15. An accurate (a) and an inaccurate (b) prediction of the ZST_BEST₁ model with 0.8 threshold. The color-coding follows Fig. 8.

B. One-shot transfer (OST)

Even though the best zero-shot transfer achieved 86.32% mAP₅₀, it had some difficulties with 4 classes. With one-shot transfer, we could overcome these difficulties. The hyperparameters of the data generation remained the same as it was described in the previous zero-shot transfer example. The difference between the two approaches lies in the data used to train the model, which is shown in Tab. IX.

With the latter approach, we achieved significantly better results. The OST_BEST₃ model achieved 97.38% mAP₅₀ on the cropped images, while the OST_BEST₁ model had 97.04% mAP₅₀ on the original images. The precision-recall curves are shown on Fig. 16 and the F₁ scores are shown in Fig. 17. The mAP scores are close to optimal and there is only insignificant deviation between the different training sessions. The F₁ score is also relatively high and flat in all cases, thus it means that the models are not sensitive to different thresholds.

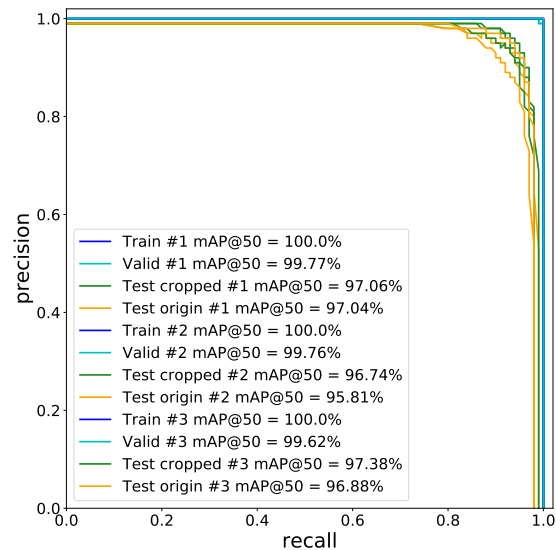


Fig. 16. The precision-recall curves of the OST_BEST models. The train and valid scores are overlapping and relatively close to the perfect 1.0 values.

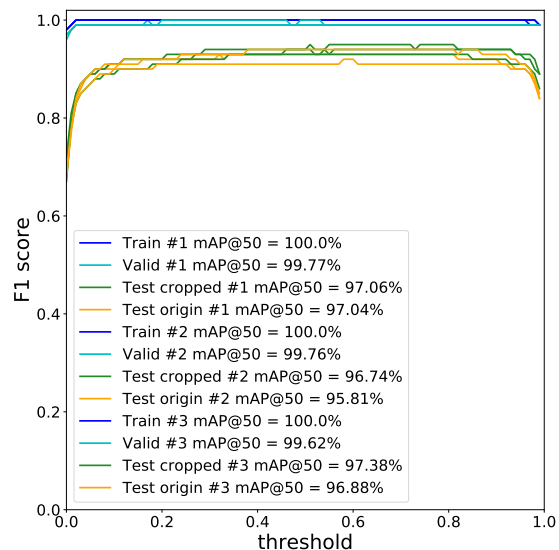


Fig. 17. The F₁ scores of the OST_BEST models.

The performance on the different types of test images is presented in Tab. X. In general, the models work well, above 94% mAP₅₀ in each case. The crowded scenes (group D) have slightly worse performance on average, but the difference is not significant.

TABLE X
THE MAP₅₀ SCORES OF THE OST_BEST MODELS IN THE DIFFERENT TEST GROUPS

ID	Train #1		Train #2		Train #3		AVG.	
	Orig.	Crop.	Orig.	Crop.	Orig.	Crop.	Orig.	Crop.
A	97.29	97.52	97.76	97.29	98.00	97.76	97.68	97.52
B	98.12	96.45	97.29	97.02	97.92	97.49	97.78	96.99
C	96.39	96.19	94.18	96.40	96.21	97.18	95.59	96.59
D	96.23	95.94	94.97	94.42	95.60	95.64	95.60	95.33
E	96.70	98.94	93.77	97.47	93.34	97.91	94.60	98.11
F	98.99	99.37	98.83	99.20	99.76	99.52	99.19	99.36

Furthermore, the mAP scores of the different classes are presented in Tab. XI and shown in Fig. 18. All classes perform well, the worst-performing class on the original images is the L-bracket with 92.62% mAP₅₀. The precision-recall curves of the OST_BEST₃ for the different classes are depicted on Fig. 19. Compared to the zero-shot approach, the curves are shifted towards the top-right corner which demonstrates better performance. The proposed confusion matrix of the OST_BEST₃ with 0.8 threshold is shown on Fig. 20. Almost all the values are in the diagonal, meaning that they are good predictions. However, some objects of L-bracket, U-bracket, and cable shoe were not found by the model. The number of false negative examples can be decreased by lowering the threshold at the expense of possible false positive examples.

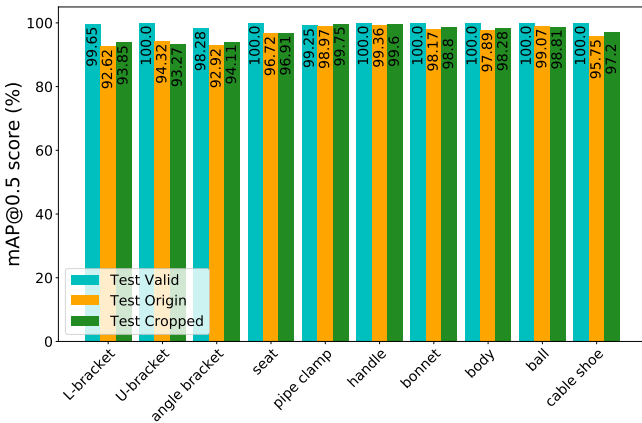


Fig. 18. The average mAP₅₀ scores of the OST_BEST models in the different classes.

For qualitative evaluation, Fig. 21 shows an accurate prediction and an inaccurate solution. In the latter case, the distractor objects that resembled in main characteristics of a body object could mislead the model. Supposedly, the model learned a too general representation of the object. As the quantitative results show, the vast majority of examples are accurate.

VIII. ABLATION STUDY

In this section, the ablation study of the method is presented, focusing on the different elements of the domain randomiza-

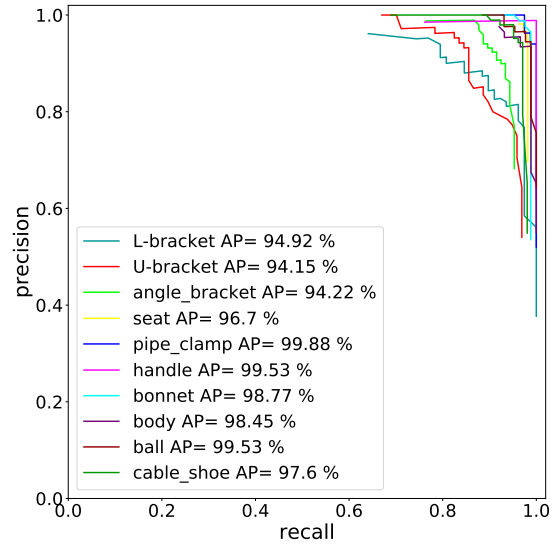


Fig. 19. Class precision recall curves of the OST_BEST₃ model on the cropped images.

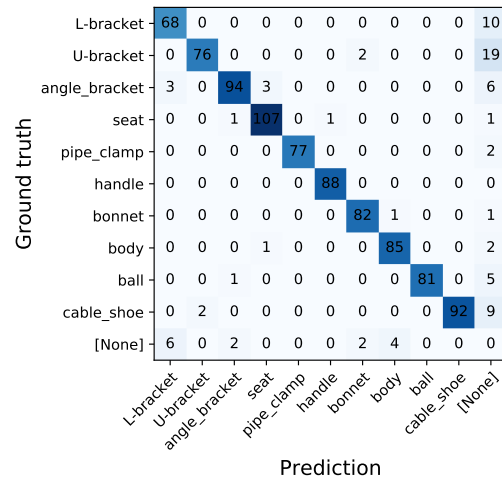


Fig. 20. Confusion matrix of the OST_BEST₃ model on the cropped images with 0.8 threshold.

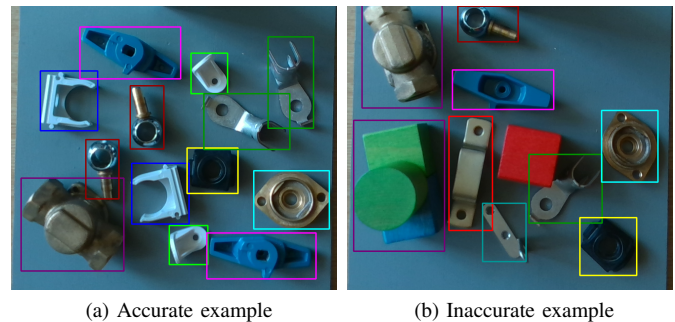


Fig. 21. An accurate (a) and an inaccurate (b) prediction of the OST_BEST₃ model with 0.8 threshold. The color-coding follows Fig. 8.

tion methods, the training data size, and the object detection model.

TABLE XI

THE MAP₅₀ SCORES OF OST_BEST MODELS FOR THE DIFFERENT CLASSES

ID	Train #1		Train #2		Train #3		AVG.	
	Orig.	Crop.	Orig.	Crop.	Orig.	Crop.	Orig.	Crop.
1	93.70	93.94	90.24	92.70	93.92	94.92	92.62	93.85
2	94.75	92.45	92.94	93.21	95.28	94.15	94.32	93.27
3	93.19	94.85	92.95	93.25	92.61	94.22	92.92	94.11
4	96.76	96.93	96.74	97.11	96.65	96.70	96.72	96.91
5	99.34	99.54	99.19	99.84	98.38	99.88	98.97	99.75
6	99.51	99.57	99.17	99.71	99.40	99.53	99.36	99.60
7	98.30	98.81	98.51	98.81	97.69	98.77	98.17	98.80
8	98.50	98.40	96.94	98.00	98.23	98.45	97.89	98.28
9	99.52	98.43	97.74	98.47	99.96	99.53	99.07	98.81
10	96.83	97.73	93.70	96.26	96.73	97.60	95.75	97.20

TABLE XII

THE MAP₅₀ SCORES OF ZST_BEST MODELS WITH DIFFERENT SEEDS

Seed	Train #1		Train #2		Train #3		AVG.	
	Orig.	Crop.	Orig.	Crop.	Orig.	Crop.	Orig.	Crop.
80725	79.71	78.67	81.93	84.55	78.30	80.69	79.98	81.30
80725	82.29	78.31	80.99	84.31	79.60	79.23	80.96	80.62
53418	83.57	80.69	78.13	80.95	74.74	76.92	78.81	79.52
16505	85.38	86.32	81.31	82.01	82.79	81.29	83.16	83.21

A. Seed

In general, the initial random seed of stochastic algorithms can significantly influence their performance. This phenomenon is unpleasant as it makes the algorithms unpredictable. We aim to measure the influence of the seed of our domain randomization method in the case of the ZST_BEST models. It is important to note that for the training, the random seed is not the same seed that we use for the domain randomization method. Tab. XII shows different seeds (with two equal seeds for reference), each with 3 independent training sessions. In these experiments, we showed that the magnitude of the deviation of the results due to the stochastic training process of the neural network and due to the different seeds of the randomized data generation methods are comparable. Thus, our randomized data generation method is not less robust to a given seed than the stochastic training method itself.

B. Texture and post-processing

Two important factors in our domain randomization method are the random textures of the objects and the post-processing method. We have generated different images without these factors. The results are summarized in Tab. XIII and the results on the original images are shown in Fig. 22. Both the added texture and the post-processing methods contribute significantly to the performance. Without the added texture, the performance drops to 63.50% and 74.71% mAP₅₀ in the case of the original and the cropped images. Without post-processing, the performance is only 55.87% and 60.42%

TABLE XIII

THE MAP₅₀ SCORES OF DIFFERENT ZST MODELS. -T: WITHOUT TEXTURE, -PP: WITHOUT POST PROCESSING, -TPP: WITHOUT POST PROCESSING AND TEXTURE.

Desc.	Train #1		Train #2		Train #3		AVG.	
	Orig.	Crop.	Orig.	Crop.	Orig.	Crop.	Orig.	Crop.
BEST	85.38	86.32	81.31	82.01	82.79	81.29	83.16	83.21
-T	62.83	73.26	61.08	74.07	66.59	76.80	63.50	74.71
-PP	61.40	63.14	50.58	60.62	55.63	57.51	55.87	60.42
-TPP	10.89	9.48	12.51	13.75	9.08	18.21	10.83	13.81

mAP₅₀, respectively. The performance decreases drastically achieving 10.83% and 13.81% mAP₅₀ without the mentioned domain randomization techniques. Thus, these experiments show how essential these types of domain randomization methods are. As the average performance of the model on the validation dataset is 99.84% mAP₅₀, according to Eq. 2, the reality gap shrinks, in case of the original images, on average from 89.01% (-TPP) to 16.68% mAP₅₀ (BEST).

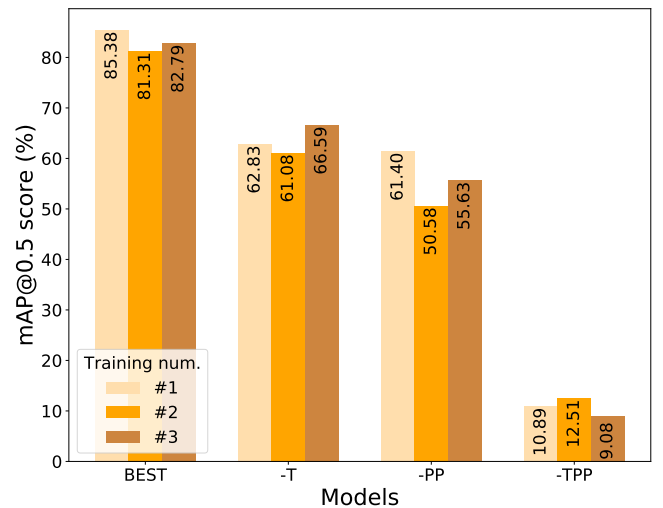


Fig. 22. Results of the ablation study on the original images (ZST models). Model without added textures (-T), without post-processing methods (-PP), and without both (-TPP).

C. Data size

The size of the training dataset is a key attribute of any machine learning problem. In general, the more data are used in the training dataset, the better its distribution will match the real probability distribution. Nevertheless, this phenomenon does not necessarily apply to the case of knowledge transfer. The results of the ZST_BEST models' performance in the case of different training data sizes are presented in Tab. XIV. It is important to note that for the case of 8000 images, the training time was doubled from 5000 to 10000 iterations. Even though increasing the training data size from 1000 to 4000 allows the model to gain notable performance, doubling the data size from 4000 to 8000 only causes marginal improvement.

TABLE XIV

THE MAP₅₀ SCORES OF ZST_BEST MODELS WITH DIFFERENT DATA SIZES

Size	Train #1		Train #2		Train #3		AVG.	
	Orig.	Crop.	Orig.	Crop.	Orig.	Crop.	Orig.	Crop.
1000	70.07	72.12	77.94	76.60	75.37	78.12	74.46	75.61
4000	85.38	86.32	81.31	82.01	82.79	81.29	83.16	83.21
8000	84.56	85.64	86.95	83.68	81.96	81.46	84.49	83.59

TABLE XV

THE MAP₅₀ SCORES OF ZST MODELS WITHOUT DIFFERENT FACTORS. -G: NO GRAVITY, -R: NO RANDOMNESS IN GRID POSITIONS AND NO GRAVITY, 8P: 8-POINT BOUNDING BOX CALCULATION

ID	Train #1		Train #2		Train #3		AVG.	
	Orig.	Crop.	Orig.	Crop.	Orig.	Crop.	Orig.	Crop.
BEST	85.38	86.32	81.31	82.01	82.79	81.29	83.16	83.21
-G	61.12	71.47	65.86	69.89	68.76	75.25	65.25	72.20
-R	49.12	63.07	62.00	74.38	48.18	69.53	53.10	68.99
8P	31.09	40.66	28.98	37.77	39.19	45.93	33.09	41.45

D. Gravity, positional disturbance, and bounding-box calculation

In this part of the ablation study, the effect of simulated gravity, the effect of random disturbance around the grid positions, and the effect of replacing the all-point bounding box calculation to the 8-point bounding box calculation (described in Section IV-B4) are measured. The findings are summarized in Tab. XV. All of the aforementioned factors have a relevant effect on the performance. In the case of cropped images, on average, gravity brings 11.01% mAP₅₀, the randomness of objects positions contributes 14.22% mAP₅₀, and the tight all-point bounding box calculation method is responsible for a 41.76% mAP₅₀ performance gain. Nevertheless, for the latter case, the performance drops with the less tight BBs seemingly because of two reasons. Firstly, the ground-truth BBs are tight, thus computing the IOU₅₀ with less tight BBs results in many discarded matches. Secondly, on the crowded images the BBs are too large, consequently, they are or would significantly overlap each other which confuses the predictor.

E. Cutouts

Some additional experiments were conducted with different types of cutouts at the post-processing phase of data generation presented in Tab. XVI. In these experiments, 4 types of cutouts were considered which are the following: rectangles, partly transparent rectangles, circles, and lines. The number of the cutouts and the bounds of the randomized sizes of the cutouts varied over the experiments. The results show that in none of the cases could we achieve a better performance than the ZST_BEST model that does not have this type of domain randomization. Nevertheless, a more thorough evaluation of the effect of different cutouts can be the subject of further research.

TABLE XVI

THE MAP₅₀ SCORES OF ZST MODELS WITH DIFFERENT CUTOPTS AT THE POST-PROCESSING METHODS

ID	Train #1		Train #2		Train #3		AVG.	
	Orig.	Crop.	Orig.	Crop.	Orig.	Crop.	Orig.	Crop.
BEST	85.38	86.32	81.31	82.01	82.79	81.29	83.16	83.21
CUT1	68.24	77.18	66.93	76.77	71.85	83.53	69.01	79.16
CUT2	82.12	78.97	78.56	83.33	72.99	69.79	77.89	77.36
CUT3	58.25	75.13	56.39	74.45	58.97	76.46	57.87	75.35
CUT4	76.00	69.76	70.17	78.62	68.26	73.60	71.48	73.99
CUT5	70.32	74.74	75.50	78.74	74.59	74.91	73.47	76.13
CUT6	78.53	76.86	74.83	79.77	79.70	82.27	77.69	79.63
CUT7	82.25	80.26	70.22	69.95	74.51	77.48	75.66	75.90
CUT8	75.64	75.63	75.58	80.46	80.96	84.06	77.39	80.05

TABLE XVII

THE MAP₅₀ SCORES OF R101-FPN FASTER R-CNN MODEL

	Zero-shot transfer		One-shot transfer	
	valid	test	valid	test
Train #1	85.90	49.78	97.18	71.97
Train #2	85.78	66.73	96.495	67.70
Train #3	86.38	55.41	96.78	70.73
AVG.	86.02	57.31	96.82	70.13

F. Faster R-CNN

To test the performance of the data generation process in the case of a two-stage object detection model, we trained the R101-FPN version of the Faster R-CNN [6] model using the Detectron2 [66] framework and Pytorch [67]. This model uses the ResNet-101 [61] model with the Feature Pyramid Network [68] backbone. The results are shown in Table. XVII. Even though the performance of the model fails behind YOLOv4, it could be increased with a more exhaustive hyperparameter search. Moreover, the Darknet framework uses extra data augmentation for training that we did not reproduce for the Detectron2 framework. Important to note, that, here as well, having one real image for training gives a considerable performance improvement.

The training of the Faster R-CNN model was approximately 4 times faster than in the case of YOLOv4. On the other hand, inference time was around 10 times slower with 2 FPS. In conclusion, YOLOv4 outperformed the Faster R-CNN approach in performance and in inference time which are the two most relevant factors.

IX. ROBOTIC APPLICATION

Object detection can be utilized in many ways. As an example, in robotic grasping or in pick-and-place applications where the robot needs to detect the different pieces and grasp them or move them to specific places.

In this section a real-world robotic implementation of our method is presented that can serve as proof of concept built

upon our previous work [69], where we proposed a 5C model-based [70] system architecture for visual servo guided cyber-physical robotic assembly cells. Having the object detection model, the parameters of the grasping (micro plan) can be computed.

The robotic system consists of a six DoF collaborative robot arm equipped with a digital depth camera, a force sensor, and a two-finger gripper. The robot's task is to detect the scattered workpieces (center points and bounding box information) as well as predict grasping positions. The sensors and actuators of the robot, and the sim2real computer vision module are connected in a robot control framework based on ROS [71]. The setup is depicted in Fig. 23 while the software components of the robot control framework are shown in Fig. 24

For robotic applications every component of the system must work not only reliably but also in real-time. In order to evaluate the sim2real computer vision module in a new case, three novel industrial parts were used depicted in Fig. 23. The data generation and training process went without any problems. Thus, within 13 hours the new model was ready to use. As a qualitative evaluation, the robot was programmed to follow a path over the workpieces while streaming the camera data. On a GeForce RTX 3060 GPU, our computer vision model ran with 20 FPS and constantly localized and classified the objects perfectly with most of the times above 98% confidence even in significantly different illumination settings and with the presence of distractor objects.

For grasping the workpieces, the grasping pose needs to be estimated and transformed to the robot coordinate system. For estimating the orientation we used principal component analysis on the detected and cropped bounding boxes of the objects and for the transformation a standard camera calibration method was applied.

This use case was presented in an exhibition² and the implementation of the ROS-based robot control system is available here: https://git.sztaki.hu/emi/robot_control_framework

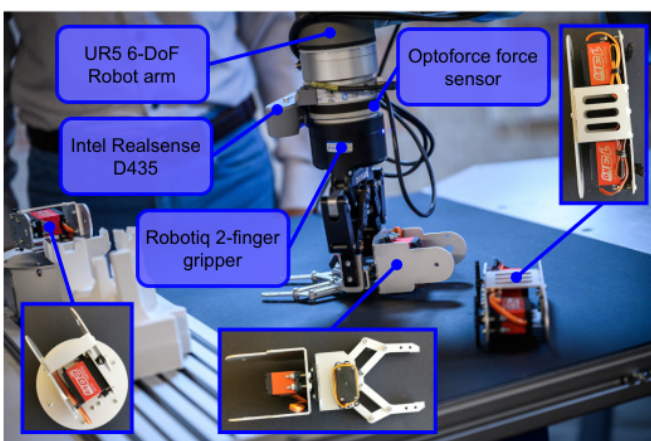


Fig. 23. The setup of the robotic application.

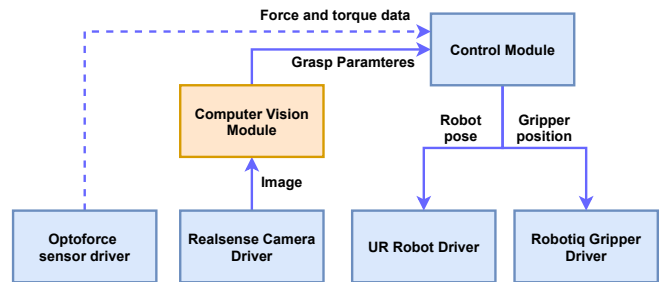


Fig. 24. The flow of information in the robotic application. With orange the computer vision module is shown which is the main topic of this paper. In this application, the force sensor was not used, shown with dashed line. The following software resources were used: [72], [73], [74], [75], [76].

X. CONCLUSION

The paper presents our sim2real domain randomization method for objects detection. As our general aim is to facilitate the trend of new-generation intelligent manufacturing with adaptive robotic applications, our solution needed to be capable of differentiating similar classes using only 1 real example for training, and working in real-time. According to our best knowledge, this is the first work thus far that mutually satisfies these constraints in this domain.

As recent works on transfer learning did not concentrate on similar objects to validate our solution, we created a dataset with 190 real annotated images of 920 objects of 10 classes of industrial workpieces that addresses this phenomenon. The dataset is publicly available and can serve as a benchmark for industrial object detection models.

We introduced a novel type of confusion matrix tailored for object detection. It is proven to be useful for finding the root cause of performance loss.

As a proof of concept, we showed that our model works reliably and real-time in a robotic pick-and-place application.

Both the sim2real data generation and training module, and the robot control framework can be used as a freely available, out-of-the-box solution to industrial problems

The results presented in the paper validate the strength of our approach. We achieved 86.32% mAP₅₀ in the case of zero-shot transfer, while with one-shot transfer, the best model scores 97.38% mAP₅₀ on the test set. With these experiments, we also demonstrated how to diminish the performance loss caused by similar classes by introducing only 1 image from the target domain. Even though it is hard to compare algorithms of different problems, we firmly believe that these results are better than the ones in the literature considering the complexity of the problem and the size of the synthetic and real training dataset.

In a thorough ablation study, we showed that adding random texture and our post-processing domain randomization methods are crucial parts of the process. We also found that simulating gravity, random initial placement, and the all-point bounding box calculating method give significant contributions to the performance.

In the future, we aim to further improve the performance of the zero-shot learning method. We are also interested

²Source: <https://youtu.be/6PhaXW1m9Xw>

in working with point cloud data, exploring the field of adversarial training, and extending our method to be able to predict end-to-end grasping poses as well.

June 20, 2022

ACKNOWLEDGMENT

This research has been supported by the ED_18-2-2018-0006 grant on an “Research on prime exploitation of the potential provided by the industrial digitalisation”

The research presented in this paper, carried out by Institute for Computer Science and Control was supported by the Ministry for Innovation and Technology and the National Research, Development and Innovation Office within the framework of the National Lab for Autonomous Systems.

The work of Tomáš Horváth was supported by the project “Application Domain Specific Highly Reliable IT Solutions” financed by the National Research, Development and Innovation Fund of Hungary (TKP2020-NKA-06), under the Thematic Excellence Programme no. 2020-4.1.1.-TKP2020 (National Challenges Subprogramme) funding scheme.

REFERENCES

- [1] J. Zhou, Y. Zhou, B. Wang, and J. Zang, “Human–Cyber–Physical Systems (HCPSs) in the Context of New-Generation Intelligent Manufacturing,” *Engineering*, vol. 5, no. 4, pp. 624–636, Aug. 2019. [Online]. Available: <https://www.doi.org/10.1016/j.eng.2019.07.015>
- [2] A. Zeng, S. Song, J. Lee, A. Rodriguez, and T. Funkhouser, “TossingBot: Learning to Throw Arbitrary Objects With Residual Physics,” *IEEE Transactions on Robotics*, vol. 36, no. 4, pp. 1307–1319, Aug. 2020. [Online]. Available: <https://doi.org/10.1109/TRO.2020.2988642>
- [3] I. Alonso, L. Riazuelo, and A. C. Murillo, “MiniNet: An Efficient Semantic Segmentation ConvNet for Real-Time Robotic Applications,” *IEEE Transactions on Robotics*, vol. 36, no. 4, pp. 1340–1347, Aug. 2020. [Online]. Available: <https://doi.org/10.1109/TRO.2020.2974099>
- [4] O. Russakovsky, J. Deng, H. Su, J. Krause, S. Satheesh, S. Ma, Z. Huang, A. Karpathy, A. Khosla, M. Bernstein, A. C. Berg, and L. Fei-Fei, “ImageNet Large Scale Visual Recognition Challenge,” *International Journal of Computer Vision*, vol. 115, no. 3, pp. 211–252, Dec. 2015. [Online]. Available: <https://doi.org/10.1007/s11263-015-0816-y>
- [5] T.-Y. Lin, M. Maire, S. Belongie, J. Hays, P. Perona, D. Ramanan, P. Dollár, and C. L. Zitnick, “Microsoft COCO: Common Objects in Context,” in *Computer Vision – ECCV 2014*, D. Fleet, T. Pajdla, B. Schiele, and T. Tuytelaars, Eds. Cham: Springer International Publishing, 2014, pp. 740–755. [Online]. Available: https://link.springer.com/chapter/10.1007/978-3-319-10602-1_48
- [6] S. Ren, K. He, R. Girshick, and J. Sun, “Faster R-CNN: Towards Real-Time Object Detection with Region Proposal Networks,” *IEEE Transactions on Pattern Analysis and Machine Intelligence*, vol. 39, no. 6, pp. 1137–1149, June 2017. [Online]. Available: <http://doi.org/10.1109/TPAMI.2016.2577031>
- [7] W. Liu, D. Anguelov, D. Erhan, C. Szegedy, S. Reed, C.-Y. Fu, and A. C. Berg, “SSD: Single Shot MultiBox Detector,” in *Computer Vision – ECCV 2016*, B. Leibe, J. Matas, N. Sebe, and M. Welling, Eds. Cham: Springer International Publishing, Sept. 2016, pp. 21–37. [Online]. Available: https://link.springer.com/chapter/10.1007/978-3-319-46448-0_2
- [8] A. Bochkovskiy, C.-Y. Wang, and H.-Y. M. Liao, “YOLOv4: Optimal Speed and Accuracy of Object Detection,” Apr. 2020. [Online]. Available: <https://arxiv.org/abs/2004.10934>
- [9] S. Levine, P. Pastor, A. Krizhevsky, and D. Quillen, “Learning Hand-Eye Coordination for Robotic Grasping with Deep Learning and Large-Scale Data Collection,” *The International Journal of Robotics Research*, Mar. 2016. [Online]. Available: <https://doi.org/10.1177/0278364917710318>
- [10] S. J. Pan and Q. Yang, “A Survey on Transfer Learning,” *IEEE Transactions on Knowledge and Data Engineering*, vol. 22, no. 10, pp. 1345–1359, Oct. 2010. [Online]. Available: <https://doi.org/10.1109/TKDE.2009.191>
- [11] K. Weiss, T. M. Khoshgoftaar, and D. Wang, “A Survey of Transfer Learning,” *Journal of Big Data*, vol. 3, no. 1, p. 9, Dec. 2016. [Online]. Available: <http://doi.org/10.1186/s40537-016-0043-6>
- [12] A. Pashevich, R. Strudel, I. Kalevatykh, I. Laptev, and C. Schmid, “Learning to Augment Synthetic Images for Sim2Real Policy Transfer,” in *2019 IEEE/RSJ International Conference on Intelligent Robots and Systems (IROS)*, Nov. 2019, pp. 2651–2657. [Online]. Available: <https://doi.org/10.1109/IROS40897.2019.8967622>
- [13] K. Bousmalis, A. Irpan, P. Wohlhart, Y. Bai, M. Kecey, M. Kalakrishnan, L. Downs, J. Ibarz, P. Pastor, K. Konolige, S. Levine, and V. Vanhoucke, “Using Simulation and Domain Adaptation to Improve Efficiency of Deep Robotic Grasping,” in *2018 IEEE International Conference on Robotics and Automation (ICRA)*, May 2018, pp. 4243–4250. [Online]. Available: <https://doi.org/10.1109/ICRA.2018.8460875>
- [14] J. Tobin, R. Fong, A. Ray, J. Schneider, W. Zaremba, and P. Abbeel, “Domain Randomization for Transferring Deep Neural Networks from Simulation to the Real World,” in *2017 IEEE/RSJ International Conference on Intelligent Robots and Systems (IROS)*, Sept. 2017, pp. 23–30. [Online]. Available: <https://doi.org/10.1109/IROS.2017.8202133>
- [15] A. Dehban, J. Borrego, R. Figueiredo, P. Moreno, A. Bernardino, and J. Santos-Victor, “The Impact of Domain Randomization on Object Detection: A Case Study on Parametric Shapes and Synthetic Textures*,” in *2019 IEEE/RSJ International Conference on Intelligent Robots and Systems (IROS)*, Nov. 2019, pp. 2593–2600. [Online]. Available: <https://doi.org/10.1109/IROS40897.2019.8968139>
- [16] D. Kingma and M. Welling, “Auto-Encoding Variational Bayes,” *2nd International Conference on Learning Representations (ICLR)*, May 2014. [Online]. Available: <https://arxiv.org/abs/1312.6114>
- [17] I. J. Goodfellow, J. Pouget-Abadie, M. Mirza, B. Xu, D. Warde-Farley, S. Ozair, A. Courville, and Y. Bengio, “Generative Adversarial Networks,” June 2014. [Online]. Available: <https://arxiv.org/abs/1406.2661>
- [18] N. Jakobi, “Evolutionary Robotics and the Radical Envelope-of-Noise Hypothesis,” *Adaptive Behavior*, vol. 6, no. 2, pp. 325–368, Sept. 1997. [Online]. Available: <https://doi.org/10.1177/105971239700600205>
- [19] K. Simonyan and A. Zisserman, “Very Deep Convolutional Networks for Large-Scale Image Recognition,” Apr. 2015. [Online]. Available: <https://arxiv.org/abs/1409.1556>
- [20] E. Todorov, T. Erez, and Y. Tassa, “MuJoCo: A Physics Engine for Model-Based Control,” in *2012 IEEE/RSJ International Conference on Intelligent Robots and Systems*, Oct. 2012, pp. 5026–5033. [Online]. Available: <https://doi.org/10.1109/IROS.2012.6386109>
- [21] J. Tobin, L. Biewald, R. Duan, M. Andrychowicz, A. Handa, V. Kumar, B. McGrew, A. Ray, J. Schneider, P. Welinder, W. Zaremba, and P. Abbeel, “Domain Randomization and Generative Models for Robotic Grasping,” in *2018 IEEE/RSJ International Conference on Intelligent Robots and Systems (IROS)*, Oct. 2018, pp. 3482–3489. [Online]. Available: <https://doi.org/10.1109/IROS.2018.8593933>
- [22] J. Borrego, R. Figueiredo, A. Dehban, P. Moreno, A. Bernardino, and J. Santos-Victor, “A Generic Visual Perception Domain Randomisation Framework for Gazebo,” in *2018 IEEE International Conference on Autonomous Robot Systems and Competitions (ICARSC)*, Apr. 2018, pp. 237–242. [Online]. Available: <https://doi.org/10.1109/ICARSC.2018.8374189>
- [23] N. Koenig and A. Howard, “Design and Use Paradigms for Gazebo, an Open-Source Multi-Robot Simulator,” in *2004 IEEE/RSJ International Conference on Intelligent Robots and Systems (IROS) (IEEE Cat. No.04CH37566)*, vol. 3, Sept. 2004, pp. 2149–2154 vol.3. [Online]. Available: <https://doi.org/10.1109/IROS.2004.1389727>
- [24] K. Perlin, “Improving Noise,” *ACM Transactions on Graphics*, vol. 21, no. 3, pp. 681–682, July 2002. [Online]. Available: <https://doi.org/10.1145/566654.566636>
- [25] E. Coumans and Y. Bai, “PyBullet, a Python Module for Physics Simulation for Games, Robotics and Machine Learning,” 2016–2017. [Online]. Available: <http://pybullet.org>
- [26] R. Coulom, “Efficient Selectivity and Backup Operators in Monte-Carlo Tree Search,” in *Computers and Games*, ser. Lecture Notes in Computer Science, H. J. van den Herik, P. Ciancarini, and H. H. L. M. J. Donkers, Eds. Springer, 2007, pp. 72–83. [Online]. Available: https://doi.org/10.1007/978-3-540-75538-8_7

- [27] T. DeVries and G. W. Taylor, "Improved Regularization of Convolutional Neural Networks with Cutout," Nov. 2017. [Online]. Available: <http://arxiv.org/abs/1708.04552>
- [28] S. James, A. J. Davison, and E. Johns, "Transferring End-to-End Visuomotor Control from Simulation to Real World for a Multi-Stage Task," Oct. 2017. [Online]. Available: <http://arxiv.org/abs/1707.02267>
- [29] A. Devo, G. Mezzetti, G. Costante, M. L. Fravolini, and P. Valigi, "Towards Generalization in Target-Driven Visual Navigation by Using Deep Reinforcement Learning," *IEEE Transactions on Robotics*, vol. 36, no. 5, pp. 1546–1561, Oct. 2020. [Online]. Available: <https://doi.org/10.1109/TRO.2020.2994002>
- [30] Epic Games, "Unreal engine." [Online]. Available: <https://www.unrealengine.com>
- [31] Y. Chen, W. Li, C. Sakaridis, D. Dai, and L. Van Gool, "Domain Adaptive Faster R-CNN for Object Detection in the Wild," in *2018 IEEE/CVF Conference on Computer Vision and Pattern Recognition*, Jun. 2018, pp. 3339–3348, iSSN: 2575-7075. [Online]. Available: <https://doi.org/10.1109/CVPR.2018.00352>
- [32] M. Johnson-Roberson, C. Barto, R. Mehta, S. N. Sridhar, K. Rosaen, and R. Vasudevan, "Driving in the Matrix: Can Virtual Worlds Replace Human-Generated Annotations for Real World Tasks?" in *2017 IEEE International Conference on Robotics and Automation (ICRA)*, May 2017, pp. 746–753. [Online]. Available: <https://doi.org/10.1109/ICRA.2017.7989092>
- [33] C. Sakaridis, D. Dai, and L. Van Gool, "Semantic Foggy Scene Understanding with Synthetic Data," *International Journal of Computer Vision*, vol. 126, no. 9, pp. 973–992, Sep. 2018. [Online]. Available: <https://doi.org/10.1007/s11263-018-1072-8>
- [34] S. Sankaranarayanan, Y. Balaji, A. Jain, S. N. Lim, and R. Chellappa, "Learning from Synthetic Data: Addressing Domain Shift for Semantic Segmentation," in *2018 IEEE/CVF Conference on Computer Vision and Pattern Recognition*, Jun. 2018, pp. 3752–3761, iSSN: 2575-7075. [Online]. Available: <https://doi.org/10.1109/CVPR.2018.00395>
- [35] G. Ros, L. Sellart, J. Materzynska, D. Vazquez, and A. M. Lopez, "The SYNTHIA Dataset: A Large Collection of Synthetic Images for Semantic Segmentation of Urban Scenes," in *2016 IEEE Conference on Computer Vision and Pattern Recognition (CVPR)*, Jun. 2016, pp. 3234–3243, iSSN: 1063-6919. [Online]. Available: <https://doi.org/10.1109/CVPR.2016.352>
- [36] S. R. Richter, V. Vineet, S. Roth, and V. Koltun, "Playing for Data: Ground Truth from Computer Games," in *Computer Vision – ECCV 2016*, ser. Lecture Notes in Computer Science, B. Leibe, J. Matas, N. Sebe, and M. Welling, Eds. Cham: Springer International Publishing, 2016, pp. 102–118. [Online]. Available: https://doi.org/10.1007/978-3-319-46475-6_7
- [37] J. Tremblay, A. Prakash, D. Acuna, M. Brophy, V. Jampani, C. Anil, T. To, E. Cameracci, S. Boochoon, and S. Birchfield, "Training Deep Networks with Synthetic Data: Bridging the Reality Gap by Domain Randomization," in *2018 IEEE/CVF Conference on Computer Vision and Pattern Recognition Workshops (CVPRW)*, Jun. 2018, pp. 1082–10828, iSSN: 2160-7516. [Online]. Available: <https://doi.org/10.1109/CVPRW.2018.00143>
- [38] A. Geiger, P. Lenz, and R. Urtasun, "Are We Ready for Autonomous Driving? The KITTI Vision Benchmark Suite," in *2012 IEEE Conference on Computer Vision and Pattern Recognition*, Jun. 2012, pp. 3354–3361, iSSN: 1063-6919. [Online]. Available: <https://doi.org/10.1109/CVPR.2012.6248074>
- [39] J. Dai, Y. Li, K. He, and J. Sun, "R-FCN: Object Detection via Region-Based Fully Convolutional Networks," in *Proceedings of the 30th International Conference on Neural Information Processing Systems*, ser. NIPS'16. Red Hook, NY, USA: Curran Associates Inc., Dec. 2016, pp. 379–387. [Online]. Available: <https://dl.acm.org/doi/10.5555/3157096.3157139>
- [40] A. Gaidon, Q. Wang, Y. Cabon, and E. Vig, "Virtual Worlds as Proxy for Multi-Object Tracking Analysis," in *2016 IEEE Conference on Computer Vision and Pattern Recognition (CVPR)*, Jun. 2016, pp. 4340–4349, iSSN: 1063-6919. [Online]. Available: <https://doi.org/10.1109/CVPR.2016.470>
- [41] S. Hinterstoisser, V. Lepetit, P. Wohlhart, and K. Konolige, "On Pre-Trained Image Features and Synthetic Images for Deep Learning," Nov. 2017. [Online]. Available: <http://arxiv.org/abs/1710.10710>
- [42] B. T. Phong, "Illumination for Computer Generated Pictures," *Communications of the ACM*, vol. 18, no. 6, pp. 311–317, Jun. 1975. [Online]. Available: <https://doi.org/10.1145/360825.360839>
- [43] F. Zhang, J. Leitner, Z. Ge, M. Milford, and P. Corke, "Adversarial Discriminative Sim-to-Real Transfer of Visuo-Motor Policies," *The International Journal of Robotics Research*, vol. 38, no. 10-11, pp. 1229–1245, Sep. 2019, publisher: SAGE Publications Ltd STM. [Online]. Available: <https://doi.org/10.1177/0278364919870227>
- [44] H. M. Clever, P. Grady, G. Turk, and C. C. Kemp, "BodyPressure – Inferring Body Pose and Contact Pressure from a Depth Image," May 2021. [Online]. Available: <http://arxiv.org/abs/2105.09936>
- [45] H. M. Clever, Z. Erickson, A. Kapusta, G. Turk, C. K. Liu, and C. C. Kemp, "Bodies at Rest: 3D Human Pose and Shape Estimation From a Pressure Image Using Synthetic Data," in *2020 IEEE/CVF Conference on Computer Vision and Pattern Recognition (CVPR)*, Jun. 2020, pp. 6214–6223, iSSN: 2575-7075. [Online]. Available: <https://doi.org/10.1109/CVPR42600.2020.00625>
- [46] S. Liu, X. Huang, N. Fu, C. Li, Z. Su, and S. Ostadabbas, "Simultaneously-Collected Multimodal Lying Pose Dataset: Towards In-Bed Human Pose Monitoring under Adverse Vision Conditions," Aug. 2020. [Online]. Available: <http://arxiv.org/abs/2008.08735>
- [47] D. F. Gomes, P. Paoletti, and S. Luo, "Generation of GelSight Tactile Images for Sim2Real Learning," *IEEE Robotics and Automation Letters*, vol. 6, no. 2, pp. 4177–4184, Apr. 2021. [Online]. Available: <https://doi.org/10.1109/LRA.2021.3063925>
- [48] B. Calli, A. Singh, A. Walsman, S. Srinivasa, P. Abbeel, and A. M. Dollar, "The YCB Object and Model Set: Towards Common Benchmarks for Manipulation Research," in *2015 International Conference on Advanced Robotics (ICAR)*, Jul. 2015, pp. 510–517. [Online]. Available: <https://doi.org/10.1109/ICAR.2015.7251504>
- [49] E. Rohmer, S. P. N. Singh, and M. Freese, "V-REP: A Versatile and Scalable Robot Simulation Framework," in *2013 IEEE/RSJ International Conference on Intelligent Robots and Systems*, Nov. 2013, pp. 1321–1326, iSSN: 2153-0866. [Online]. Available: <https://doi.org/10.1109/IROS.2013.6696520>
- [50] J. Lee, M. Grey, S. Ha, T. Kunz, S. Jain, Y. Ye, S. Srinivasa, M. Stilman, and K. Liu, "DART: Dynamic Animation and Robotics Toolkit," *The Journal of Open Source Software*, vol. 3, p. 500, Feb. 2018. [Online]. Available: <https://doi.org/10.21105/joss.00500>
- [51] M. Macklin, M. Müller, N. Chentanez, and T.-Y. Kim, "Unified Particle Physics for Real-Time Applications," *ACM Transactions on Graphics*, vol. 33, no. 4, pp. 153:1–153:12, Jul. 2014. [Online]. Available: <https://doi.org/10.1145/2601097.2601152>
- [52] M. Matl, "Pyrender." [Online]. Available: <https://github.com/mmatl/pyrender>
- [53] Z. Zou, Z. Shi, Y. Guo, and J. Ye, "Object Detection in 20 Years: A Survey," May 2019. [Online]. Available: <http://arxiv.org/abs/1905.05055>
- [54] R. Girshick, J. Donahue, T. Darrell, and J. Malik, "Rich Feature Hierarchies for Accurate Object Detection and Semantic Segmentation," in *2014 IEEE Conference on Computer Vision and Pattern Recognition*, June 2014, pp. 580–587. [Online]. Available: <https://doi.org/10.1109/CVPR.2014.81>
- [55] K. He, X. Zhang, S. Ren, and J. Sun, "Spatial Pyramid Pooling in Deep Convolutional Networks for Visual Recognition," in *Computer Vision – ECCV 2014*, ser. Lecture Notes in Computer Science, D. Fleet, T. Pajdla, B. Schiele, and P. Tuytelaars, Eds. Springer International Publishing, 2014, pp. 346–361. [Online]. Available: https://doi.org/10.1007/978-3-319-10578-9_23
- [56] R. Girshick, "Fast R-CNN," in *2015 IEEE International Conference on Computer Vision (ICCV)*, Dec. 2015, pp. 1440–1448, iSSN: 2380-7504. [Online]. Available: <https://doi.org/10.1109/ICCV.2015.169>
- [57] J. Redmon, S. Divvala, R. Girshick, and A. Farhadi, "You Only Look Once: Unified, Real-Time Object Detection," in *2016 IEEE Conference on Computer Vision and Pattern Recognition (CVPR)*. IEEE, June 2016, pp. 779–788. [Online]. Available: <https://doi.org/10.1109/CVPR.2016.91>
- [58] J. Redmon and A. Farhadi, "YOLO9000: Better, Faster, Stronger," in *2017 IEEE Conference on Computer Vision and Pattern Recognition (CVPR)*. IEEE, July 2017, pp. 6517–6525. [Online]. Available: <https://doi.org/10.1109/CVPR.2017.690>
- [59] —, "YOLOv3: An Incremental Improvement," Apr. 2018. [Online]. Available: <https://arxiv.org/abs/1804.02767>
- [60] T.-Y. Lin, P. Goyal, R. Girshick, K. He, and P. Dollár, "Focal Loss for Dense Object Detection," *IEEE Transactions on Pattern Analysis and Machine Intelligence*, vol. 42, no. 2, pp. 318–327, Feb. 2020. [Online]. Available: <https://doi.org/10.1109/TPAMI.2018.2858826>
- [61] K. He, X. Zhang, S. Ren, and J. Sun, "Deep Residual Learning for Image Recognition," in *2016 IEEE Conference on Computer Vision and Pattern Recognition (CVPR)*, June 2016, pp. 770–778. [Online]. Available: <https://doi.org/10.1109/CVPR.2016.90>
- [62] M. Cimpoi, S. Maji, I. Kokkinos, S. Mohamed, and A. Vedaldi, "Describing Textures in the Wild," in *2014 IEEE Conference on Computer Vision and Pattern Recognition*, June 2014, pp. 3606–3613,

ISSN: 1063-6919. [Online]. Available: <https://doi.org/10.1109/CVPR.2014.461>

- [63] “Free Stock Textures.” [Online]. Available: <https://freestocktextures.com/>
- [64] “Texture Ninja.” [Online]. Available: <http://textureninja.com>
- [65] E. Angel and D. Shreiner, *Interactive Computer Graphics: A Top-Down Approach with WebGL*, 7th ed. Boston: Pearson, Feb. 2014.
- [66] Y. Wu, A. Kirillov, F. Massa, W.-Y. Lo, and R. Girshick, “Detectron2,” 2019. [Online]. Available: <https://github.com/facebookresearch/detectron2>
- [67] A. Paszke, S. Gross, F. Massa, A. Lerer, J. Bradbury, G. Chanan, T. Killeen, Z. Lin, N. Gimelshein, L. Antiga, A. Desmaison, A. Kopf, E. Yang, Z. DeVito, M. Raison, A. Tejani, S. Chilamkurthy, B. Steiner, L. Fang, J. Bai, and S. Chintala, “Pytorch: An Imperative Style, High-Performance Deep Learning Library,” in *Advances in Neural Information Processing Systems 32*. Curran Associates, Inc., 2019, pp. 8024–8035. [Online]. Available: <http://papers.nips.cc/paper/9015-pytorch-an-imperative-style-high-performance-deep-learning-library.pdf>
- [68] T.-Y. Lin, P. Dollár, R. Girshick, K. He, B. Hariharan, and S. Belongie, “Feature Pyramid Networks for Object Detection,” in *2017 IEEE Conference on Computer Vision and Pattern Recognition (CVPR)*, Jul. 2017, pp. 936–944, ISSN: 1063-6919. [Online]. Available: <https://doi.org/10.1109/CVPR.2017.106>
- [69] G. Erdős, D. Horváth, and G. Horváth, “Visual Servo Guided Cyber-Physical Robotic Assembly Cell,” *IFAC-PapersOnLine*, vol. 54, no. 1, pp. 595–600, Jan. 2021. [Online]. Available: <https://doi.org/10.1016/j.ifacol.2021.08.068>
- [70] J. Lee, B. Bagheri, and H.-A. Kao, “A Cyber-Physical Systems Architecture for Industry 4.0-based Manufacturing Systems,” *Manufacturing Letters*, vol. 3, pp. 18–23, Jan. 2015. [Online]. Available: <https://doi.org/10.1016/j.mfglet.2014.12.001>
- [71] Stanford Artificial Intelligence Laboratory et al., “Robotic Operating System.” [Online]. Available: <https://www.ros.org>
- [72] “ROS Wrapper for Intel® RealSense™ Devices.” [Online]. Available: <https://github.com/IntelRealSense/realsense-ros>
- [73] “Universal Robots ROS Driver.” [Online]. Available: https://github.com/UniversalRobots/Universal_Robots_ROS_Driver
- [74] F. Exner, “Universal Robot.” [Online]. Available: https://github.com/fmauch/universal_robot
- [75] D. Ordóñez, “Robotiq 2-Finger Grippers.” [Online]. Available: https://github.com/Danfoa/robotiq_2finger_grippers
- [76] Tossy, “YOLO V4 for Darknet ROS.” [Online]. Available: https://github.com/Tossy0423/yolov4-for-darknet_ros



Dániel Horváth received his M.Sc. degree in mechatronics from the Budapest University of Technology and Economics in 2019, spending one-one semesters at the Technical University of Denmark in Copenhagen and at the Otto von Guericke University in Magdeburg.

He is pursuing his Ph.D. at the Eötvös Loránd University (ELTE), Budapest in computer science in collaboration with the Research Laboratory on Engineering and Management Intelligence of the Institute for Computer Science and Control in Budapest under

the supervision of Gábor Erdős, Zoltán Istenes, and Tomáš Horváth. His main research areas are computer vision, transfer learning, robotic grasping, and mobile robots



Gábor Erdős received his M.Sc. degree in mechanical engineering from the State University of New York at Buffalo in 1995 and his Ph.D. degree from the Budapest University of Technology and Economics in 2000. He is a postdoctoral researcher at the École Polytechnique Fédérale de Lausanne, Switzerland until 2002.

He joined the Institute for Computer Science and Control, Budapest as a researcher in 2003 and since 2018, he is the deputy head of the Research Laboratory on Engineering and Management Intelligence.

His main research fields are robotics, point-cloud and 3D modeling, digital twin models, multi-body kinematics, and virtual manufacturing.



Zoltán Istenes received his Ph.D. degree in Informatics in 1997 from the University of Nantes.

He is working ever since at the Eötvös Loránd University, Faculty of Informatics (ELTE, Budapest, Hungary) as an associate professor. Between 2008 and 2020 he was the manager of the Budapest EIT Digital Doctoral School. He is the founder of the ELTE Faculty of Informatics Robotics Lab.

His main teaching and research interests include computer architectures, artificial intelligence, expert systems, robotics, IoT, UAVs, formal methods, and

recently autonomous self-driving vehicles.



Tomáš Horváth received his Ph.D. degree at Pavol Jozef Šafárik University in Košice, Slovak Republic, in 2008. He was a post-doc researcher at the University in Hildesheim, Germany, and at the University of São Paulo, Brazil.

He is the head of the Data Science and Engineering Department at the Faculty of Informatics of the Eötvös Loránd University in Budapest, Hungary, and also a faculty member of the Institute of Computer Science at the Faculty of Science of Pavol Jozef Šafárik University.

His research interests include relational learning, pattern mining, recommender systems, meta-learning, and automated machine learning.



Sándor Földi received his B.Sc. degree in Mechatronics from the Budapest University of Technology and Economics in 2021.

He joined the transfer learning project at the Research Laboratory on Engineering and Management Intelligence in the Institute for Computer Science and Control in 2020. He has previously participated in the work of the Antal Bejczy Center for Intelligent Robotics at the Óbuda University. His main research fields are computer vision, transfer learning, and generative adversarial networks.